Seismicity Patterns in the Hengill area in South West Iceland

Diploma thesis submitted in partial fulfilment
of the requirements for the degree of
Diplom-Geophysiker

at the

Institute of Geophysics and Geology
Universität Leipzig

by

Christoph Sens-Schönfelder

August, 2003

Tutors:
Michael Korn, Universität Leipzig
Ragnar Stefánsson, Icelandic Meteorological Office

Contents

Preface

The earthquake process has always attracted much attention. Earthquakes pose a hazard to thousands of people which is especially frightening due to their sudden occurrence and destructive potential. Not only because of this there is great scientific interest in a theoretical description but also classical mechanics fails to describe the high complexity of the earthquake process which is governed by complex interactions of various non-linear processes acting on vastly different space and time scales. A comprehensive understanding of the earthquake dynamics as a whole is still a goal of the future (e.g. Main, 1999).

So far earthquake seismology has been restricted to study various sorts of patterns in the seismicity (cf. Wyss, 1999). The first group of patterns emerged during the search for precursors of large earthquakes. Such are for example Mogi doughnuts, seismic gaps, precursory quiescence, precursory activation and temporal clustering. The Mogi doughnut is an early example observed by Mogi (1969) that describes a doughnut shaped ring of anomalous high activity that develops within decades before a large earthquake occurs in its quiet interior. A comparable phenomenon is described by the terms seismic gap and precursory quiescence which state that the spatially and temporally less active segments of a fault are the most likely places for large earthquakes.

The second group of seismicity patterns is studied in order to infer some information about the rupturing crust rather than about the earthquake process itself. These patterns include spatial and temporal variability of scaling parameters that describe the frequence-magnitude distribution or the spatial and temporal clustering of seismicity. The theoretical and experimental background for interpretation of these patterns is sometimes ambiguous and needs further development. Recently a third group of non-local seismic patterns appeared in the literature. In opposite to older, local approaches the new rely on the concept of critical point dynamics which implies long range correlations. Goltz (2001) used an approach from remote sensing called Principal Component Analysis to decompose spatio-temporal seismicity patterns

into independent constituents in order to separate subtle precursory patterns from stronger irrelevant patterns. Tiampo (2002) applied the concept of mean-field threshold systems from statistical mechanics to earthquake data to forecast space time patterns of seismic activity.

In this work I aim at studying patterns of the second group. In terms of studying crustal properties and processes I think this is the most promising way to utilize the information contained in earthquake catalogues.

Chapter 1

Introduction

1.1 Tectonic setting of Iceland

The relatively simple geometry of the rift/transform systems of the Mid-Atlantic Ridge (MAR) is completely disturbed as it approaches the Icelandic mainland. The elevation of the MAR spreading axis rises from about 2 km below sea level to more than 1 km above sea. This is due to the Iceland Hot Spot that feeds the extensive volcanism which has build up the thick Icelandic crust. The MAR is represented by the Kolbeinsey Ridge (KR) north of Iceland and by the Reykjanes Ridge (RR) to the south (figure 1.1). The total spreading rate in South Iceland averages to about 2 cm per year (DeMets et al., 1994) with a direction of 100° from north.

The volcanism in Iceland is concentrated in three neovolcanic zones, the Northern, Western and Eastern Volcanic Zones (NVZ, WVZ, EVZ), that represent the accretion axis. Additionally there are three flank zones with poorly developed extensional features (Sæmundsson, 1986). The location of the volcanic zones is determined by the movement of the North Atlantic rift system relative to the Iceland Hot Spot. According to the HS2-NUVEL 1 absolute plate motion model (Gripp and Gordon, 1990) the Eurasian plate moves over the hot spot towards SSW with a velocity of 0.8 cm per year, causing an offset of the ridge from the hot spot of about 0.3 cm per year. The tendency of the rift system to maintain its position on top of the magma source is reflected in repeated rift jumps (Sæmundsson, 1986).

North of 65° latitude the last rift jump moved the spreading axis from the line that connects the WVZ with the KR to the presently active NVZ. In south Iceland a rift jump is thought to be in progress. It transfers the crustal spreading from the older and almost inactive WVZ to the younger and southward propagating EVZ (Einarsson and Eiríksson, 1982). Since this

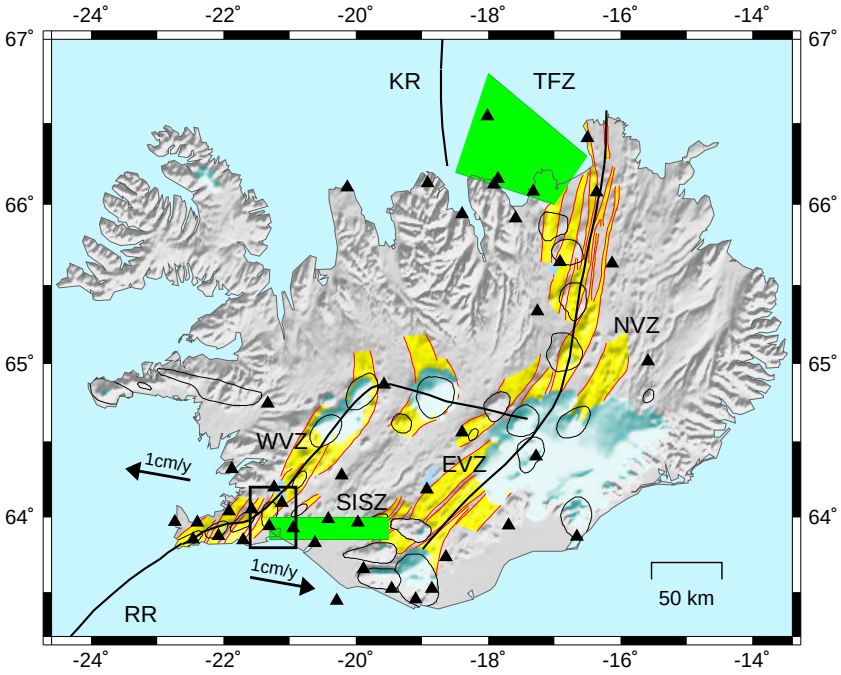

Figure 1.1: Tectonic setting of Iceland (after Einarsson and Sæmundsson (1987)). Abbreviations are explained in the text. Yellow denotes fissure swarms. Central volcanoes are irregularly shaped black circles. Green denotes Fracture Zones. Black lines indicate extensional plate boundary. Arrows indicate spreading direction and triangles stations of the seismic network. Box shows location of study area at the triple junction between the Reykjanes Peninsula oblique rift (onland continuation of RR) the WVZ and the SISZ. See figure 1.2 for closeup.

rift jump can not be considered finished there are two parallel rift systems in south Iceland. This setting of the rift systems is indicated by the black lines in figure 1.1. It shows that the plate boundary in the Iceland region is offset about 150 km from the offshore ridges.

Two fracture zones have developed that bridge this offset. The Tjörnes Fracture Zone (TFZ) north of Iceland is marked by three seismic belts with WNW to NW trend. Several destructive earthquakes occurred within this zone in the last century. Fault planes identified with relative relocation of groups of events strike parallel to the trend of the fracture zone in most parts of the dominant seismic belt, but lots of small fault planes have been found to strike NNE (Rögnvaldsson et al., 1998a).

The South Iceland Seismic Zone (SISZ) accommodates the transform motion between the EVZ and the Reykjanes peninsula which is the onland

continuation of the RR. Major earthquakes occur in sequences at average intervals of 80-100 years (Einarsson, 1991). Two $M_w = 6.5$ earthquakes in June 2000 marked the last such sequence. Though the geometric relationship of the SISZ would suggest a continuous left-lateral EW fault, the deformation is taken up by right-lateral movement on numerous N trending faults and counterclockwise rotation of the blocks in between (Einarsson, 1991). This mechanism is called bookshelf-faulting.

The Reykjanes peninsula is an oblique spreading zone where the direction of the spreading axis differs up to 45° from the direction of opening. Seismicity along the peninsula revealed some characteristics of transform motion similar to the SISZ, especially after the SISZ events in 2000. Two $M \approx 5$ events on the Reykjanes peninsula were dynamically triggered by shear waves from the first SISZ event and another one occurred some minutes later. All three ruptured faults trending roughly N (Vogfjöð, 2003; Pagli et al., 2003).

The complex structures of the fracture zones in Iceland can be seen as a response to the unstable situation of the rift zones (Einarsson, 1991). Faults perpendicular to the direction of deformation and bookshelf faulting were observed as transient features in the development of a major shear fault (Cox and Scholz, 1988).

At the juncture between the Reykjanes peninsula, the SISZ and the WVZ the Hengill triple junction is located which is the target of this work (black box in figure 1.1).

1.2 Tectonics of the Hengill Triple Junction

The Hengill Triple Junction is named after the topographically and geologically dominant Mount Hengill (803 m). Together with its transecting fissure swarm that extends form the coast south of Hengill to north of Lake Thingvallavatn (Th) the Hengill cental volcano (He) forms the respective volcanic system. It is the focus of the main volcanic production in this area. The associated high-temperature geothermal system is being utilized in the Nesjavellir power plant at the south coast of Lake Thingvallavatn.

At the eastern edge of the Hengill volcanic system there is another less pronounced system which constitutes a separate focus of volcanic production. The geothermal activity of this system is most intense at Ölkelduháls a few kilometers south of its central volcano mount Hrómundartindur (Hr). A third system that is far less active than Hrómundartindur or Hengill is the volcanic system of the extinct Grensdalur central volcano (Gr).

The geothermal activity of these systems is expressed in numerous hot springs and fumaroles that occur widespread in the area around the central

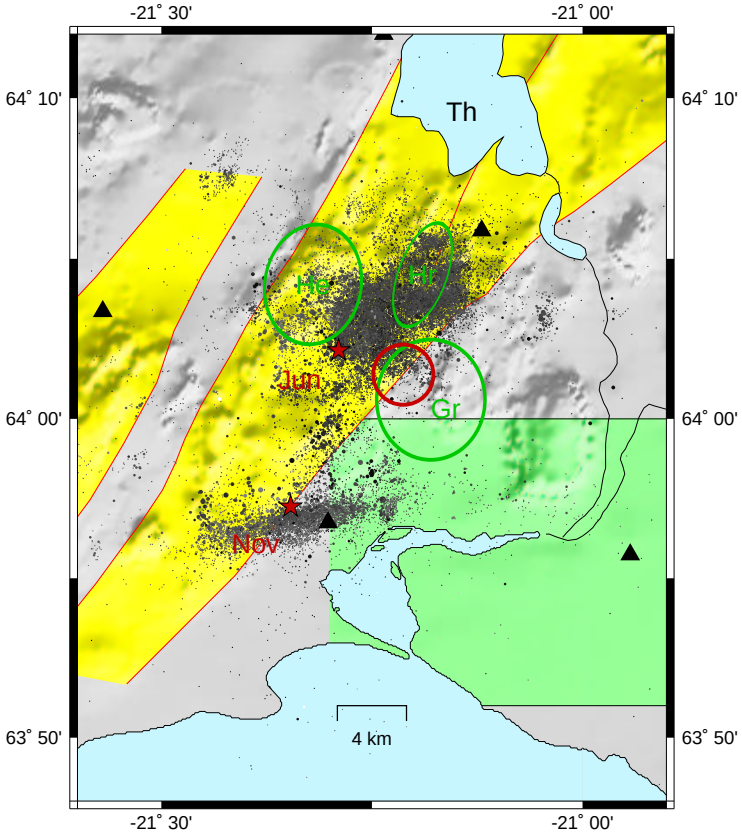

Figure 1.2: Tectonic setting of the Hengill triple junction. Abbreviation are explained in the text. The approximate location of the three central volcanoes are indicated as ellipsoids. Red circle shows center of uplift estimated by (Feigl et al., 2000). Points show epicenters of $M_L > 0.5$ events of the period 1993-2000. Stars indicate the two $M_L \approx 5$ events from 1998.

volcanoes.

The recent tectonic activity is bound to the Hengill volcanic system since the center of volcanic productions has shifted from Grensdalur to the Hengill system some 0.5 Ma ago. Except for a smaller Hengill eruption in 1789 the last major volcanic eruption occurred about 2000 years ago (Sæmundsson, 1995). Rifting is documented in 9000 years old lava flows that are transect by the a fissure swarm north of lake Thingvallavatn with a total dilatation of about 100 m (Guðmundsson, 1987). This accounts for about half of the 2 cm/yr spreading rate in south Iceland in post glacial times. The last significant rifting episode accompanied the 1789 eruption. During the last 35 years no significant dilatation could be measured in geodetic surveys across the

Hengill fissure swarm. This clarifies the relocation process of the spreading center from the WVZ to the EVZ.

Average subsidence of the Hengill fissure swarm occurred at a rate of 4 mm/yr during the last 10000 years (Rögnvaldsson et al., 1998b). In 1789 the last major tectonic episode caused considerable ground deformations and was accompanied by 10 days of continuous seismic activity and single events that were felt during several months. Between 1952 and 1955 several earthquake swarms occurred in the Hengill area and ended with a magnitude 5.5 event in 1955 (Rögnvaldsson et al., 1998b). Since then the seismic activity in the Hengill area has remained on a relatively low level until 1994.

In 1994 intensive swarm activity started in the Hengill area beneath the Hrómundartindur central volcano. The activity began with a sequence of several thousand events above magnitude 0.5 in July 1994. In March 1995 a period of constantly high activity began, that also effected the Ölfus area about 10km south of the Hengill and Hroómundartindur central volcanoes. The event rate increased by a factor of more than ten compared to the pre-1994 activity. This period lasted until mid-1996 and the activity returned almost to the pre-1994 level until another group of sequences started in mid 1997 that culminated in two $M_L \approx 5$ events in June and November 1998. Mid-1999 activity returned again to approximately the pre-1994 level.

Repeated geodetic measurements between 1986 and 1995 detected uplift and expansion around mount Hrómundartindur that is consistent with a pointlike pressure source in 6.5 ± 3 km depth (Sigmundsson et al., 1997). Feigl et al. (2000) used interferometric analysis of synthetic aperture radar images (InSAR) to study the interaction of magmatic injection and faulting in the 1993-1998 period. They locate the point source that best explains the interferograms further south but still consistent with the source estimated by Sigmundsson et al. (1997). The inferred rate of maximum uplift is fairly constant at 19.2 ± 2 mm/yr and the source depth amounts to 7 ± 2 km. A minor magmatic injection into the roots of the Hrómundartindur volcanic system is regarded as cause of the pressure source (Sigmundsson et al., 1997; Feigl et al., 2000). Different interpretations assume fluid accumulation as source of the uplift.

The extensive seismic response to this rather small pressure source reflects the ambient stress level in the Hengill area. Fault planes determined from groups of accurately relocated events show either NS or EW oriented vertical planes and focal mechanisms indicate a NE direction of the maximum horizontal compression (Rögnvaldsson et al., 1998b). This indicates together with the fact that most earthquakes have strike-slip characteristics that the events are triggered in a previously stressed crust.

The earthquakes were detected by the South Iceland Lowland (SIL) net-

work. The SIL system is described by Stefánsson et al. (1993) and Böðvarsson et al. (1996). Currently the network consists of more than 40 three-component seismic stations (black triangles in figures 1.1 and 1.2) that are connected to a common data center in Reykjavík. There are five stations in the closer vicinity of the Hengill earthquakes. Two of them were installed in October 1996 during the study period. This improved the location estimates from typically $\pm 1 - 1.5$ km horizontally and 4 km vertically to $\pm 1 - 1.5$ both horizontally and vertically (Rögnvaldsson et al., 1998b).

Chapter 2

Declustering

Events in an earthquake catalogue are described by their hypocenter, i.e. their location in three dimensional space, their source time, and some measures for their size, i.e. different sorts of magnitude values. Fixing one sort of magnitude to be used the catalogue represents a set of points in a five dimensional space.

In this chapter I try to reveal structures in this set by declustering. The idea of declustering is to identify dependent earthquakes (clusters) according to some physical model of earthquake interaction. Typically the seismicity identified via this method is then removed from the catalog. The biggest event in each cluster remains in the catalog which then contains only independent events. In opposite to this I mainly aim at investigating the clusters individually. Thus the term *declustering* is a bit misleading, but since the procedure of identifying dependent events is the same I stick to the commonly used term *declustering*.

Other terms that will be used frequently are *sequence*, *swarm* and *cluster*. I use the term *sequence* to refer to a temporally dense succession of earthquakes without any constraint on their distribution in space and size. The term *cluster* is used for sequences that are clustered not only in time but also in space. Finally the term *swarm* is used for large clusters without an outstanding mainshock (cf. Fischer and Horálek, 2002).

Two different approaches to the problem of declustering were used. I call the first one *conventional* because it is based on deterministic assumptions about the stress redistribution that governs the interaction between earthquakes. This method has some shortcomings that are discussed below. The second approach is called *statistical* because no assumptions are made about the actual process that causes the interaction of earthquakes. Rather I use the observed statistical distributions of events in time, space and size to distinguish between interacting and independent events in a statistical sense.

2.1 Conventional method

Identification of dependent seismicity mainly aims at the foreshock – mainshock – aftershock relation because this is by far the most dominant type of earthquake interaction (Reasenberg, 1985). Various methods have been suggested to model the aftershock zones. Gardner and Knopoff (1974) for example used rectangular windows $0 < \delta t < T$ for the time distance δt between mainshock and aftershock and $0 < \delta r < R$ for their spatial distance δr, where T and R are functions of the main shock magnitude. Savage (1972) formed clusters from events separated in time and space less than some constant limits. The Single-Link-Cluster technique described by Frohlich and Davis (1990) successively connects the nearest neighbor events to small cluster then the nearest small clusters to larger clusters and so on until a certain level. This can be done in three dimensional Euclidean space or by incorporating the time via some kind of velocity in four dimensional space.

2.1.1 Description of the Algorithm

A more advanced technique was suggested by Reasenberg (1985). He based his method of identifying aftershocks on a physical two-parameter model of earthquake interaction. A spatial and a temporal interaction zone is calculated for each event in the catalogue in order to consider an event as an aftershock if it occurs within these time and space limits of an earlier event. The spatial interaction zone, i.e. the volume that is assumed to be effected by the stress redistribution after an earthquake scales with the earthquake's source dimension. The temporal interaction zone is set to a fixed value in the technique of Reasenberg (1985).

My first approach is apart from minor modifications that will be discussed later similar to the one by Reasenberg (1985). I calculate the two interaction zones and associate two events to form one cluster if the later one falls into these zones of the first one. For the development of the clusters I apply the following three rules.

- If an event that does not yet belong to a cluster is associated with an already clustered event it becomes a member of that cluster.
- If an event that already belongs to a cluster is associated with an event that belongs to another cluster the two clusters are joined together.
- When two not yet clustered events are associated they form a new cluster.

The source dimension which is the basis for the spatial interaction zone is estimated as the radius $r(M_0)$ of a circular crack that would release the same seismic moment M_0 as the earthquake. $r(M_0)$ is given by

$$r(M_0) = \sqrt[3]{\frac{7}{16} \cdot \frac{M_0}{\Delta\sigma}} \tag{2.1}$$

(Shearer, 1999) where $\Delta\sigma$ is the stress drop that I take to $\Delta\sigma = 30bar$. I derive the seismic moment from the moment magnitude M_w using $\log M_0 = 1.5M_w + 16.1$ (Lay and Wallace, 1995) where M_0 has the dimension $dyncm$ ($1dyncm = 10^{-7}Nm$). The radius of the interaction zone $R(M_0)$ is simply $r(M_0) \cdot Q$ where Q is a scaling factor. This results in the following expression for the radius of the spatial interaction zone

$$R(M_w) = Q \cdot \sqrt[3]{\frac{7}{16} \cdot \frac{(10^{1.5M_w+9.1})Nm}{(30 \cdot 10^5)\frac{N}{m^2}}} \tag{2.2}$$

which can be simplified to

$$R(M_w) = Q \cdot 0.24 \cdot 10^{(1.5M_w+4.1)/3}. \tag{2.3}$$

For the magnitude dependent time limit $T(M_w)$ I use a different approach than Reasenberg. I apply a formula used by Kagan (1999):

$$T(M_w) = W \cdot \frac{10}{3} \cdot 10^{2/3(M_w-4)} \tag{2.4}$$

which is an estimate for the time that is necessary to wait in order to observe a certain percentage of aftershocks, assuming an Omori decay. W is a scaling factor for the time limit. The two parameters W and Q allow to adjust the time and space windows in order to account for regional characteristics of the seismicity. Figure 2.1 shows the sizes of the resulting time and distance windows.

2.1.2 Modifications compared to the Reasenberg (1985) algorithm

This algorithm contains two modifications compared to the original one described in Reasenberg (1985) that should be mentioned explicitly.

- All events are treated equally.
- The length of the time window depends continuously on magnitude.

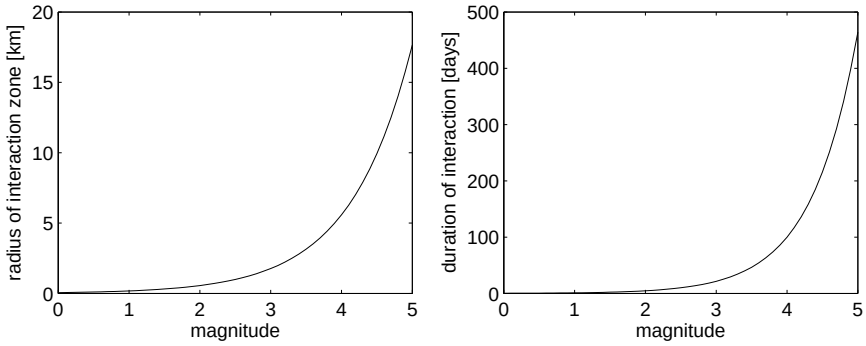

(a) Spatial interaction zone (b) Temporal interaction zone

Figure 2.1: Size of the interaction zones in time and space for the two parameters $Q = 10$ and $W = 30$.

The first modification refers to the question which earthquakes interact. In the clustering procedure, Reasenberg (1985) only considers the most recent event and the largest event in the developing cluster as triggering events conversely I consider all previous events as sources for stress modifications that lead to another event. Thereby I avoid to identify the mainshocks explicitly which is of great importance because of the swarm activity without distinctive mainshocks. However, due to the relationship between the magnitude and interaction zone the largest events have by far the strongest impact.

The second modification is adopted from Kagan (1999). Reasenberg (1985) originally used constant time windows of one day for non clustered events and ten days for clustered events. The modification was necessary because the activity in the Hengill area contains sequences with rather small temporal distance of only a few days. These sequences get connected when the numerous small events ($M_L < 1.5$) that constitute some kind of background activity have the same interaction time window as the larger events ($M_L > 2$) that dominate formation of the sequences.

2.1.3 Performance

For the sake of computational effectiveness I applied the algorithm to a dataset composed only of events with $M_L > 0.5$ to assess the performance of the algorithm. The results will be representative for the dataset including all events because the very small events below $M_L = 0.5$ do only play a passive role in the clustering process. The performance of the algorithm can

be assessed in terms of the spatio-temporal distribution of the independent and dependent seismicity and in terms of the composition of individual clusters. Independent seismicity is represented on the one hand by the events that are not associated with any cluster and on the other hand by the moment weighted centers of the clusters. Because of the moment weighting these cluster centers essentially represent the hypocenter and the origin time of the largest event. The magnitude assigned to the cluster centers corresponds to the collective seismic moment of the cluster. The events that are associated with a cluster constitute the dependent seismicity.

I use the following three criteria to decide which combination of the parameters Q and W gives the *best* results.

- According to Reasenberg (1985) the independent seismicity should be randomly distributed in time and space.
- The dependent part should resemble the main structures in the seismicity.
- The shape of individual clusters should be compact in space and time, i.e. a cluster should represent a single sequence on one fault.

To demonstrate the effect of the model parameters, some examples of the independent and dependent parts of the seismicity for some choices of the tested parameters Q and W are plotted in figures 2.2 and 2.3. At first one can see that the dependence of the algorithm on the model parameters Q and W is remarkably weak on a linear scale. Both parameters have to be varied over two orders of magnitude to go from the domain of weak clustering (low values of Q and W) where the seismicity appears to be independent to the domain of strong clustering (high values of Q and W) where seismicity appears dependent. Based on criteria one and two and visual inspection of figures 2.2 and 2.3 the best value for Q is around 10 and for W between 30 and 300.

After investigating the dependence of the temporal distribution of dependent and independent seismicity and the dependence of the shape of several clusters I fixed the values of $Q = 10$ and $W = 30$. With these values the algorithm meets the expectations that are formulated in the three criteria above quite well. The cumulative number of dependent and independent events is shown in figure 2.4 for this combination of Q and W. It is obvious that the independent events in figure 2.4(b) occur almost randomly in time which is represented by the almost constant slope between 1995 and 1998. On the other hand the dependent seismicity plotted in figure 2.4(a) exhibits a strong clustering in time.

2.1.4 Shortcomings

Though the algorithm explained above is frequently used in the literature (e.g. Kagan, 1999; Zöller and Hainzl, 2001) it rests on intuitive assumptions rather than on a rigorous physical background. Further on there are two main practical disadvantages.

One is the dependence on *two* parameters. The influence of the parameters Q and W on the number of dependent and independent events is similar i.e. there is a trade off between these two. Therefore it is necessary to investigate the shape of individual clusters in order to resolve the trade off between the size of the time and space windows.

The second disadvantage is that the space window is constant over time as long as time window lasts. The effect of this is especially evident for the two large $M_L \approx 5$ events in 1998. In these cases the radius of the spatial interaction zone is $18km$ and contains large parts of the active area. That means that the independent seismicity is almost turned off for the approximately one year period of the time window (figure 2.4(b)). This is in contradiction to criterion one in section 2.1.3 which demands a constant rate of independent seismicity.

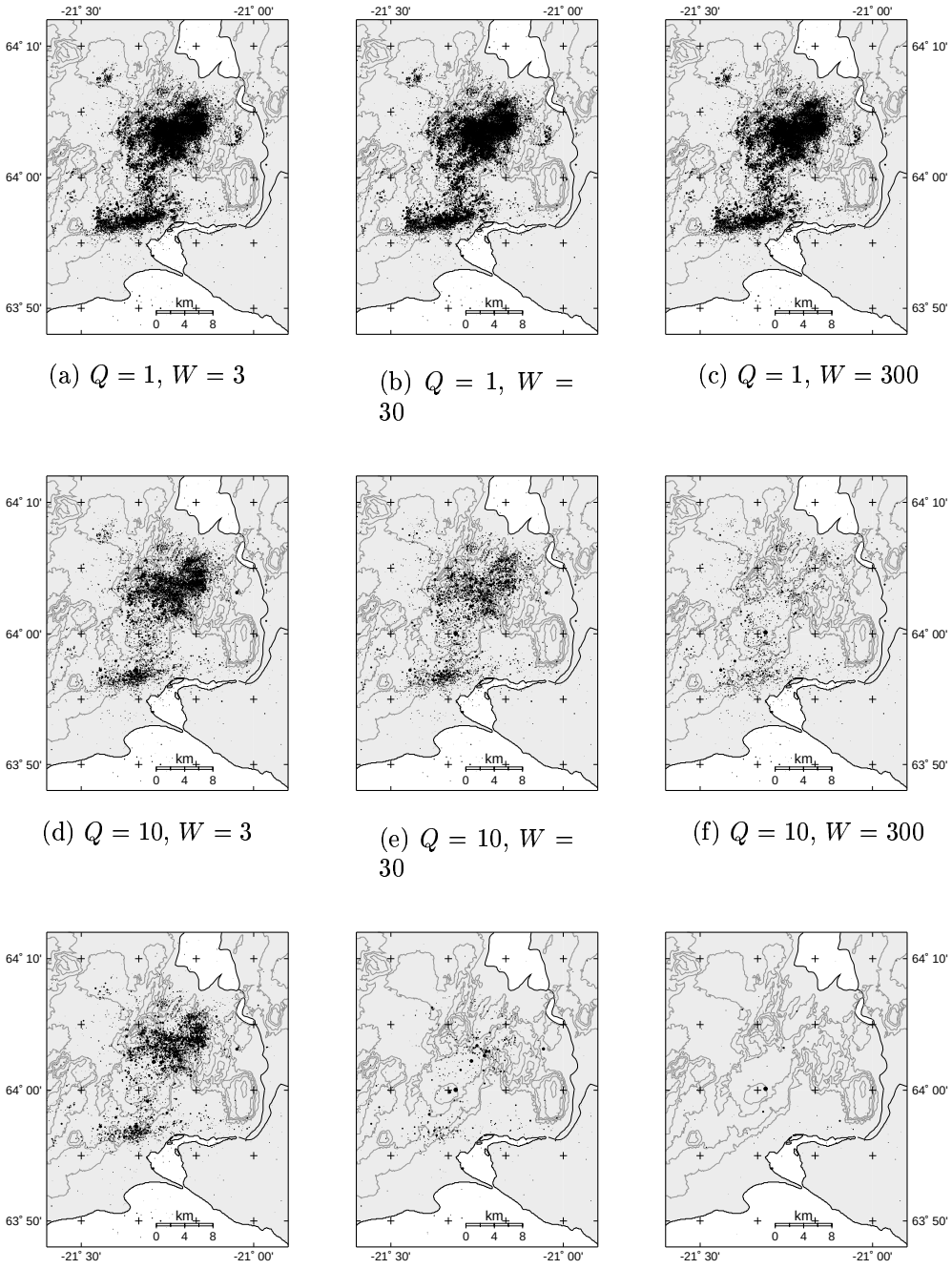

(a) $Q = 1$, $W = 3$

(b) $Q = 1$, $W = 30$

(c) $Q = 1$, $W = 300$

(d) $Q = 10$, $W = 3$

(e) $Q = 10$, $W = 30$

(f) $Q = 10$, $W = 300$

(g) $Q = 100$, $W = 3$

(h) $Q = 100$, $W = 30$

(i) $Q = 100$, $W = 300$

Figure 2.2: Independent seismicity as result of different choices of the parameters Q and W.

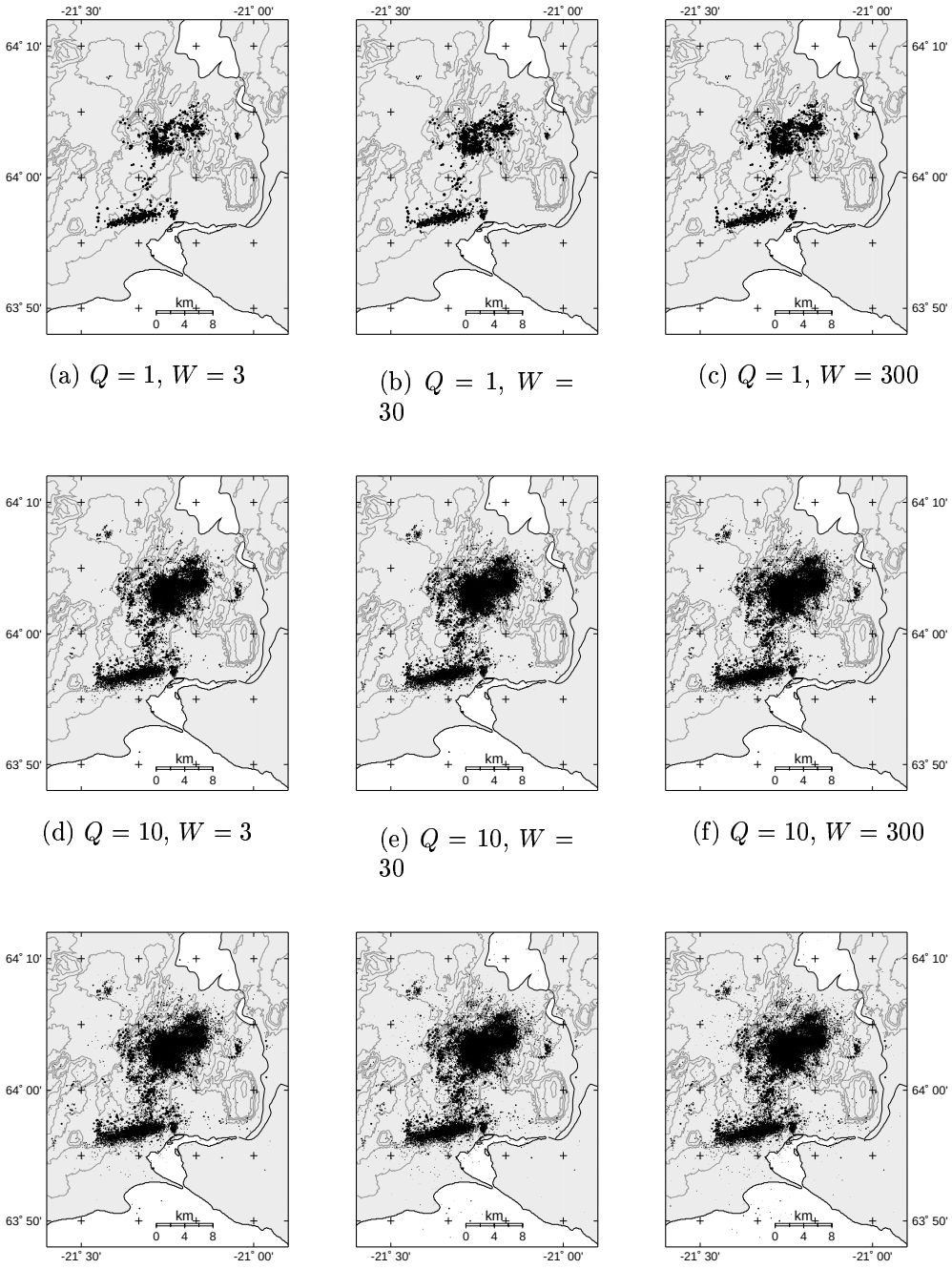

(a) $Q = 1$, $W = 3$

(b) $Q = 1$, $W = 30$

(c) $Q = 1$, $W = 300$

(d) $Q = 10$, $W = 3$

(e) $Q = 10$, $W = 30$

(f) $Q = 10$, $W = 300$

(g) $Q = 100$, $W = 3$

(h) $Q = 100$, $W = 30$

(i) $Q = 100$, $W = 300$

Figure 2.3: Dependent seismicity as result of different choices of the parameters Q and W.

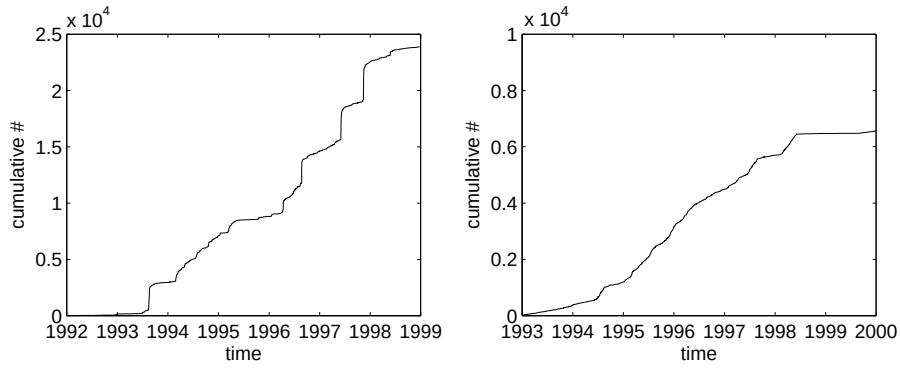

(a) Dependent seismicity (b) Independent seismicity

Figure 2.4: Cumulative number plots of dependent and independent seismicity identified using parameters $Q = 10$ and $W = 30$

2.2 Statistical method

The algorithm discussed in section 2.1 assumes a model of how stress is redistributed after an earthquake. Based on this model deterministic statements are made about which event was triggered and which was not. This is obviously a very crude approximation to the mechanisms that cause the time and space clustering of earthquakes and results in the shortcomings mentioned in section 2.1.4.

Some of these drawbacks can be overcome by using observed statistical relations between earthquakes rather than a deterministic model to describe the triggering process. A way to do so is provided by the recent finding of a unified scaling law (Bak et al., 2002).

2.2.1 Unified Scaling Law

Introduction

There are three well known relations that describe a part of the complex spatio-temporal earthquakes process.

- The size distribution of earthquakes follows the Gutenberg-Richter law (Gutenberg and Richter, 1944). It states that the number of earthquakes (N) with magnitudes greater than m is given by

$$\log_{10} N = a - bm \tag{2.5}$$

  with the constants a and $b \approx 1$. With $S = 10^m$ this can be written as

$$N \propto S^{-b}. \tag{2.6}$$

- Over short times the temporal correlation between earthquakes is given by the Omori law (Stein and Wysession, 2003) which gives the rate R of aftershocks at time T after the mainshock as

$$R \propto T^{-p} \tag{2.7}$$

  with the parameter $p \approx 1$.

- The geometry of fault systems and the distribution of epicenters is fractal (Okubo and Aki, 1987). This means the average number of epicenters N in non empty boxes of side length L is given by (cf. Goltz, 1998)

$$N \propto L^{d_f} \tag{2.8}$$

  where d_f is the fractal (capacity) dimension that ranges between 1.0 and 2.0.

The benefit of the work by Bak et al. (2002) is that it relates the three equations 2.6, 2.7 and 2.8 given above.

Waiting time statistics

In order to verify the results and to find regional distinctions I carry out the same type of analysis for the Hengill area as Bak et al. (2002) did for Southern California. Basis for this analysis is the time interval between two successive events which is also called interevent time, waiting time or as done by Bak et al. (2002) first return time.

The probability distribution of the waiting times $P(t_w)$ is defined as the probability of finding an event at time $t + t_w$ in the catalogue after the last event had occurred at time t. It can take two characteristic forms. One is the exponential form and the other one is a power law form. In the first case the exponential decay of the interevent time distribution is a sign of random occurrence of the events that can be modeled as a Poisson process. The events occur independently of each other. The power law form in contrast is a sign of temporal correlations between the events. This means the events are clustered in time, i.e. it is much more probable to measure an event just after another one than to find a significant gap between to events. The latter form is typically observed for earthquakes. Since there is strong evidence that earthquakes are self–organized critical phenomena (Bak and Tang, 1989) that usually show random occurrence of events the time-correlation among the earthquakes might be due to correlations in the driving forces (Sánchez et al., 2002).

The probability distribution of the waiting times for the Hengill events with $M_L > 0.5$ is plotted in figure 2.5(a). A strait line is fitted to the double logarithmic data according to $P(t_w) \propto t_w^{\alpha}$. The extent of the power law regime, i.e. the region where the data can be fitted by a power law is indicated. The discrepancy between the power law and the data towards shorter interevent times is due to the resolution limits of the seismic network. This means the network fails to detect events if there is a shorter time distance between the $M_L > 0.5$ events than 40 seconds. Towards longer waiting times the deviation from the power law behavior reflects the transition to an uncorrelated regime in agreement with an exponential decay. For comparison figure 2.5(b) shows how the probability distribution of interevent times would look like if the events would occur at random, i.e. without any temporal correlation. It is calculated from a synthetic catalogue of the original length that contains the same number of events as the real data set but with source times drawn from a set of uniformly distributed random numbers. The curve in figure 2.5(b) is given by $P(t_w) = T^{-1} \exp(-t_w/\bar{t_w})$ where T is the time span

of the catalogue and $\bar{t_w}$ is the average waiting time. This shape is expected for a poissonian distribution.

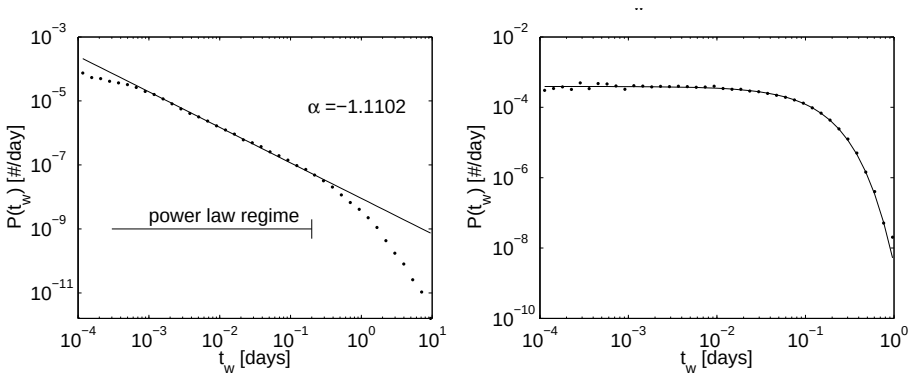

(a) Original Hengill data (b) Random time catalogue

Figure 2.5: Probability distributions of the interevent times of the Hengill data set with a lower magnitude cut of $M_L > 0.5$ and the same for a similar catalogue but with random event times drawn from a uniform distribution.

Parameterised waiting time statistics

In view of the unified scaling law especially the point where the earthquakes lose their temporal correlation, i.e. the end of the indicated power law regime in figure 2.5(a), is of great interest. Bak et al. (2002) show that the position of this point depends in a systematic way on the lower magnitude cut and on the size of the area covered by the catalogue. The systematics is revealed by introducing the parameterised probability $P_{S,L}(t_w)$ for the interevent times found in a catalogue of spatial extend L containing events greater S with $\log_{10}(S) = m$.

For this, the study area was divided into boxes of variable side length $L = 34, 17, 8.5$ and $4.25km$ as shown in figure 2.6. Size levels corresponding to a lower magnitude cut at $M_L = 0.5, 1, 1.5$ and 2 were chosen to reveal the dependence on S. $P_{S,L}(t_w)$ was then measured as follows:

1. Values for L and S were selected

2. The probability distribution of the waiting times $P(t_w)$ as defined above was estimated for the events greater than S in each cell, i.e. a histogram of the waiting times for the events greater than S contained in a particular cell was calculated.

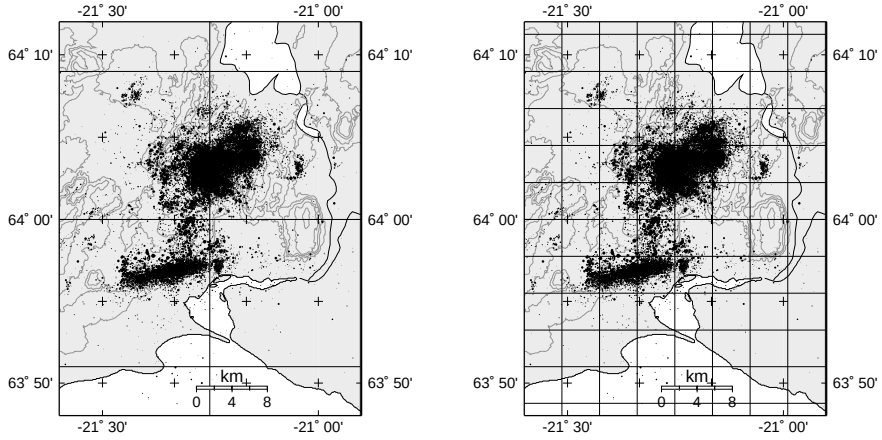

(a) Cell size $L = 17km$ (b) Cell size $L = 4.25km$

Figure 2.6: Hengill region covered with cells for the estimation of the parameterised waiting time distribution $P_{S,L}(t_w)$

3. The histograms of the various cells were combined by adding the counts in the individual bins of all the histograms.

4. To achieve comparability the combined histogram is normalised, i.e. the value of each bin of the combined histogram was divided by the sum of the counts in the histogram.

5. The procedure was repeated for all combinations of L and S.

Steps 3 and 4 represent the stacking and normalisation of the histograms. The outcome of this process is a set of 16 waiting time histograms representing $P_{S,L}(t_w)$. Eight of these waiting time distributions are plotted in figure 2.7. These plots have the same characteristics as the plot in figure 2.5(a). They consist of a linear part corresponding to the power law regime that represents the correlated regime and a faster decaying part in the uncorrelated regime. The waiting time where the transition between the two regimes occurs increases for increasing magnitude cut S (c.f. figure 2.7(a)) and decreasing region size L (c.f. figure 2.7(b)). The arrows in figure 2.7 mark these transitions for the various values of S and L.

This behaviour can be understood quite intuitively. Considering the blue curve in figure 2.7(a) it means that an event typically belongs to a new

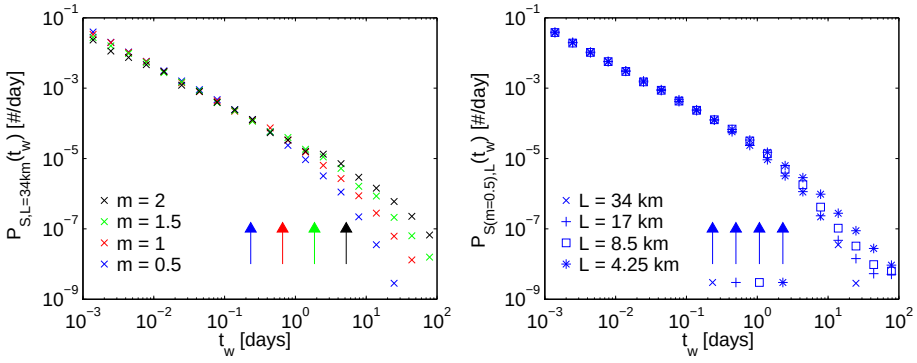

(a) Fixed length scale (b) Fixed magnitude cut

Figure 2.7: Probability distributions of waiting times for lower magnitude cut $m = 0.5, 1, 1.5, 2$ with fixed $L = 34km$ and for $L = 34, 17, 8.5, 4.25km$ with fixed $m = 0.5$. Arrows mark the transition from the correlated to the uncorrelated regime.

sequence if the time passed since the last event is larger than $0.1days$ (blue arrow). If one would only look at the events larger than 1.5 (green curve) the time gap has to be larger than $2days$ (green arrow) to mark the onset of a new sequence. This means larger events are correlated over larger time periods than are smaller events. Mathematically expressed this reads

$$P_{S,L=34km}(t_w) \propto t_w^{\alpha} g(t_w S^{-b}) \tag{2.9}$$

where b is an exponent characterising the size effect and $g(x)$ is a scaling function consisting of a constant part for arguments smaller than a critical value x_c and a typical exponentially decaying part for larger arguments.

Similarly the "$\times$" symbols in figure 2.7(b) represent a catalog of spatial extent of $34km$. The characteristic time gap for the beginning of a new sequence is $0.1day$ ("$\times$" arrow). Looking at subsets of the catalogue that do only cover a region of $8.5km$ side length ("$\star$" symbols in figure 2.7(b)) the time gap has to be $1day$ ("$\star$" arrow) to say that the latter event belongs to a new sequence. Consequently the events in smaller regions, i.e. close-by events are correlated over larger times than events in larger regions, i.e. farther separated events. This can also be expressed in a formula

$$P_{S(m=0.5),L}(t_w) \propto t_w^{\alpha} g'(t_w L^{d_f}) \tag{2.10}$$

with g' being a scaling function and d_f an exponent that describes the spatial effect.

Unified Description

As suggested by Bak et al. (2002) equations 2.9 and 2.10 can be unified to a single formula that describes space, size and time effects together. They propose equation 2.11 for the distribution of waiting times between earthquakes exceeding $S = 10^m$ in an area of side length L.

$$P_{S,L}(t_w) \propto t_w^{\alpha} f(t_w L^{d_f} S^{-b}) \tag{2.11}$$

where f is a scaling function as described above and α, d_f and b are parameters that have to be fitted.

The validity of equation 2.11 can be tested as follows. The histograms of the parameterised waiting time distribution $P_{S,L}(t_w)$ (see figures 2.7(a) and 2.7(b)) are multiplied by $t_w^{-\alpha}$ and plotted as functions of the rescaled argument $x = t_w L^{d_f} S^{-b}$. In the case that equation 2.11 holds all the data points should collapse onto a single curve that depicts the scaling function $f(x)$. Figure 2.8 shows the resulting graph for values of $\alpha = 1.1$, $d_f = 1.1$ and $b = 0.9$ which are experimentally fitted to the best data collapse. The

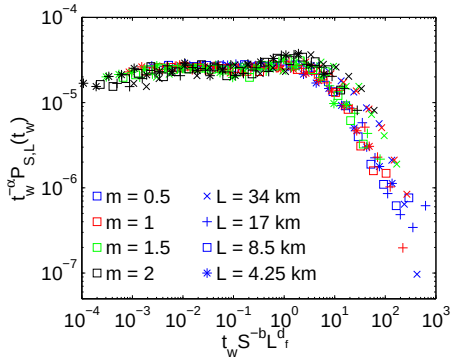

Figure 2.8: The parameterised waiting time distributions $P_{S,L}(t_w)$ multiplied by t_w^{α} as functions of the rescaled argument $t_w L^{d_f} S^{-b}$. The values $\alpha = 1.1$ (c.f. figure 2.5(a)), $d_f = 1.1$ and $b = 0.9$ have been used.

data collapses onto a single curve that fulfills the expectation for the scaling function $f(x)$. The curve is constant over more than 4 magnitudes for values of $x < 4$ and rapidly decays in accordance with an exponential function for values of $x > 4$. The constant part corresponds to the correlated regime with the t_w^{α} behaviour in figures 2.7(a) and 2.7(b) and the decaying part belongs to the uncorrelated regime with random occurrence of earthquakes. That the transition between these two regimes occurs for different values of S and L at the same (transition) point $x_c = 4$ proves the validity of equation 2.11.

To gain some insight into the uncertainties of the experimentally fitted parameters b and d_f, two further examples with different parameters are shown in figure 2.9. The effect of the parameter α is simply to change the slope of the constant part of $t_w^\alpha P_{S,L}(t_w)$ in figure 2.8 and is of no importance. To illustrate the effect of d_f, figure 2.9(a) shows $t_w^\alpha P_{S,L}(t_w)$ for the scaling exponents $b = 0.9$ and $d_f = 1.2$. The curves are multiplied by a L-dependent factor to separate curves with different L. There is a small but noticeable shift of the position of the kink as indicated by the arrows. The same applies to the effect of the scaling parameter b illustrated in figure 2.9(b). It shows $P_{S,L}(t_w)$ multiplied by a S-dependent factor for the parameters $b = 1.1$ and $d_f = 1.1$. Changes in the scaling exponents b and d_f of the order of 0.1

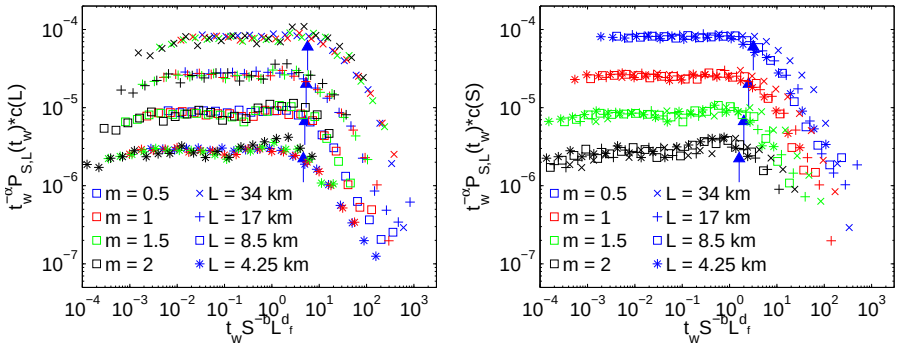

(a) $b = 0.9$, $d_f = 1.2$ (b) $b = 1.1$, $d_f = 1.1$

Figure 2.9: The parameterised waiting time distributions $P_{S,L}(t_w)$ multiplied by t_w^α as functions of the rescaled argument $t_w L^{d_f} S^{-b}$ for suboptimal values of the scaling exponents b and d_f. Curves with different L in (a) and different S respective m in (b) are shifted apart for better comparison.

or 0.2 have noticeable effects on the data collapse. The uncertainty is thus approximately ± 0.1 to ± 0.2.

Several conclusions can be drawn from equation 2.11 and figure 2.8

- The decision as to whether two events are correlated depends only on the variable $x = t_w L^{d_f} S^{-b}$ and not on S, L or t_w separately.
- The position of the kink (x_c) marks the transition from the correlated to the uncorrelated regime in the sense explained above.
- There is no difference to be made between mainshocks and aftershocks.

- The independently fitted values of d_f and b correspond to the fractal dimension and the b-value of the Gutenberg – Richter law.

Comparison with the results of Bak et al. (2002)

Since the above described analysis is the same as performed by Bak et al. (2002) a comparison seem desirable. In general my results support the findings of Bak et al. (2002) very nicely. A difference, however, is related to the different datasets. Because of the larger catalogue, which spans 16 years and contains 80000 events above their completeness level ($m = 2$), Bak et al. (2002) can trace the constant part of the scaling function $f(x)$ over more than 6 orders of magnitude of the rescaled variable x providing better confidence in the results. The transition between the correlated and the uncorrelated regimes at the kink in figure 2.8 occurs at $x_c = 4$ in units of *days* and *km*. It corresponds to the value of $x_{cB} = 10^4$ found by Bak et al. (2002) in units of *seconds* and *degrees latitudes*. The value of Bak et al. (2002) in units of *days* and *km* is $x_{cB} = 20$. Thus there is a difference of a factor 5 between the results for the Hengill region and South California. Since there are no other studies dealing with this topic, nothing is known about the influences on x_c so far. Comparison between Hengill and Californian data however suggests that the value of x_c can not be regarded universal. The difference between x_c and x_{cB} seems to be caused by regional effects in these very different environments.

2.2.2 Description of the Algorithm

As described above the concept of the unified scaling law for earthquakes provides a means to distinguish between correlated and uncorrelated activity. I used this concept to design an algorithm that finds correlated sequences i.e. groups of events that are correlated to each other. The algorithm works similar to the one described in section 2.1 except that the decision whether two particular events are interacting is now based on the unified scaling law rather than on assumptions about stress redistribution.

To use the unified scaling law (equation 2.11) to answer the question whether two particular events are correlated three minor assumptions are necessary:

- The euclidian distance between the hypocenters of two earthquakes can be used to characterise the length range L.

- The magnitude of the first earthquake characterises the size S

- The time distance between two events characterises the respective waiting time t_w in equation 2.11.

Using these assumptions it is straightforward to apply equation 2.11 in the form

$$t_w^{\alpha} P_{S,L}(t_w) \propto f(t_w L^{d_f} S^{-b}). \tag{2.12}$$

The value of $x = t_w L^{d_f} S^{-b}$ is calculated using the three assumptions above and compared to x_c, the value of the transition between the correlated and the uncorrelated regime. For $x < x_c$ the two events are associated to form a cluster, for $x \geq x_c$ they are not associated. The evolution of the clusters follow the rules given in section 2.1.1. A flowchart that represents the algorithm can be found in appendix A.

The relation between size S, length range L, and time distance t_w for a fixed value of x_c is illustrated in figure 2.10 which shows $t_w = t_w(L, S)_{x_c}$. The hight of the surface represents the maximum time that may have past after an event of size S to associate an event at distance L with it. For a magnitude 4 earthquake this means that all events closer than for example $10km$ are considered aftershocks if they occur within the next 3.5 years (green dot in figure 2.10).

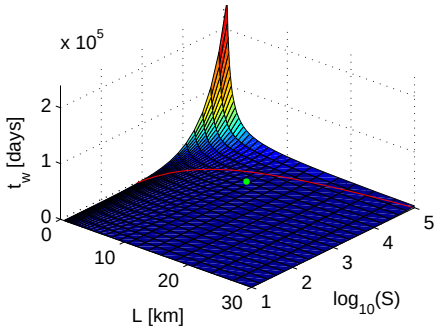

Figure 2.10: Relation between size S, length range L and time distance t_w for the value $x_c = 4$. The red line marks $t_w = 2555days$, i.e. the time span of the catalogue. Refer to text for explanation of green dot.

2.2.3 Problems and Modifications

I analyzed the dataset with the algorithm described above using the value of $x^1 = 4$ as given by the kink in figure 2.8. According to the three criteria given

[1]Hereafter is use simply x instead of x_c to denote the transition from the correlated to the uncorrelated regime.

in section 2.1.3 the results are unsatisfactory. The whole activity, except a few events that stay isolated, is associated to one single cluster.

However, this result could have been expected from figure 2.10. The red line in figure 2.10 marks the combinations of S and L that yield $t_w = 2555 days$. This time interval covers the whole time span of the dataset from 1993 to 2000.

I thus introduce two modifications. At first equation 2.12 yields an infinite time interval t_w for earthquakes located at the same position, i.e. with the same hypocenter. I avoid this singularity by introducing a minimum distance between two earthquakes equal to the approximate location errors of $0.5km$. This had no effect on the result. The second modification concerns the value of the parameter x. Obviously the position of the kink in figure 2.8 cannot directly be used in equation 2.12. I see two reasons for this fact.

At first the assumption that the hypocentral distance between two events can be used as an estimate for the length range L seems to be an oversimplification. In the calculations of the parameterised waiting time distribution in section 2.2.1 L was the side length of a square containing events of this length range. The mean distance between two events inside this square, however, is significantly smaller. In two dimensions the mean distance between two random points drawn form a uniform distribution inside a square of side length a is roughly $0.52a$ (cf. appendix B). This value decreases further when fractality of the point distribution is considered (cf. appendix B) as it is the case for epicenters. Therefore the distance between two earthquakes has to be divided by 0.5 or an even smaller value to be comparable to the length range L used in equation 2.12. I can account for this in the declustering algorithm by multiplying the value of $x = 4$ as given by the kink in figure 2.8 by $0.5^{1.1}$. This leads to a corrected value $x = 1.8$.

Using the corrected value of $x = 1.8$ does not change the result significantly. Still almost all earthquakes are associated to one cluster. I conclude that there is a difference between the statistical correlation represented by the value x and the type of clustering I look for.

The temporal correlation between earthquakes is caused by a correlation of the triggering mechanisms (Sánchez et al., 2002; Hainzl, 2003). The correlation among earthquakes identified with the concept of the Unified Scaling Law is thus related to correlated triggering, i.e. a common driving mechanism responsible for the initiation of the rupturing processes. In complex tectonic systems such as the Hengill area there is a variety of processes capable to act as such correlated triggering mechanism. Plate motion, magmatic inflation, stress transfer, viscous coupling and pore-pressure perturbations are such processes. All of these processes act on different scales, in time as well as in space.

How the algorithm handles these different types of correlations can be understood by examining the conditions that lead to the separation of the activity into different clusters 1 and 2. There is essentially one condition resulting from the description in section 2.2.2. It states that every event from cluster 1 has to be uncorrelated with all events from cluster 2. Thus the algorithm is sensitive to correlations on all scales. The correlations on the largest scale will therefore dominate the clustering process in that different clusters formed by small scale correlations are combined because of correlations over longer time-space scales.

This has two implications. At first it means that there is a triggering process common to the whole dataset from 1993 to 2000 that causes correlation over this time span in the study area. This is not really surprising since this period is characterised by extraordinarily high activity that presumably has its common cause in the interplay between magmatic activity and deformation due to plate motion. The second implication is that small scale correlations are hidden in the large clusters. However, the x-value in equation 2.12 governs the space–time scale of the correlations that lead to clustering. By reducing the corrected value of $x = 2$ as given by the unified scaling law I can exclude the large scale correlations from the clustering process. Hence I can regard the x-value as a free parameter of the clustering algorithm that allows me to set a maximum scale to the correlations that contribute to the clustering. The resulting clusters will be composed of strongly correlated events.

2.2.4 Performance

I used events with $M_L > 0.5$ and tried different values of the parameter x and assessed the results with regard to the third criterion in section 2.1.3. The other two criteria are not useful in this context because I consider strongly clustered event and the clusters are therefore only independent with regard to correlations below a certain scale. Thus I can not expect the independent seismicity to be completely randomly distributed. Again the algorithm is remarkably insensitive to changes of x on a linear scale. Therefore I used the logarithmically distributed values $1, 0.3, 0.1, 0.03$ and so on. Figure 2.11 and 2.12 show the independent and dependent parts of the seismicity for the various values of x.

Figure 2.11 nicely images the effect of reducing the correlation scale. The number of the independent events grows as the maximum correlation scale is reduced because the events within clusters of initially correlated events become uncorrelated and break up the clusters when the largest correlation scales are ignored. Simultaneously the fault structures of the area become

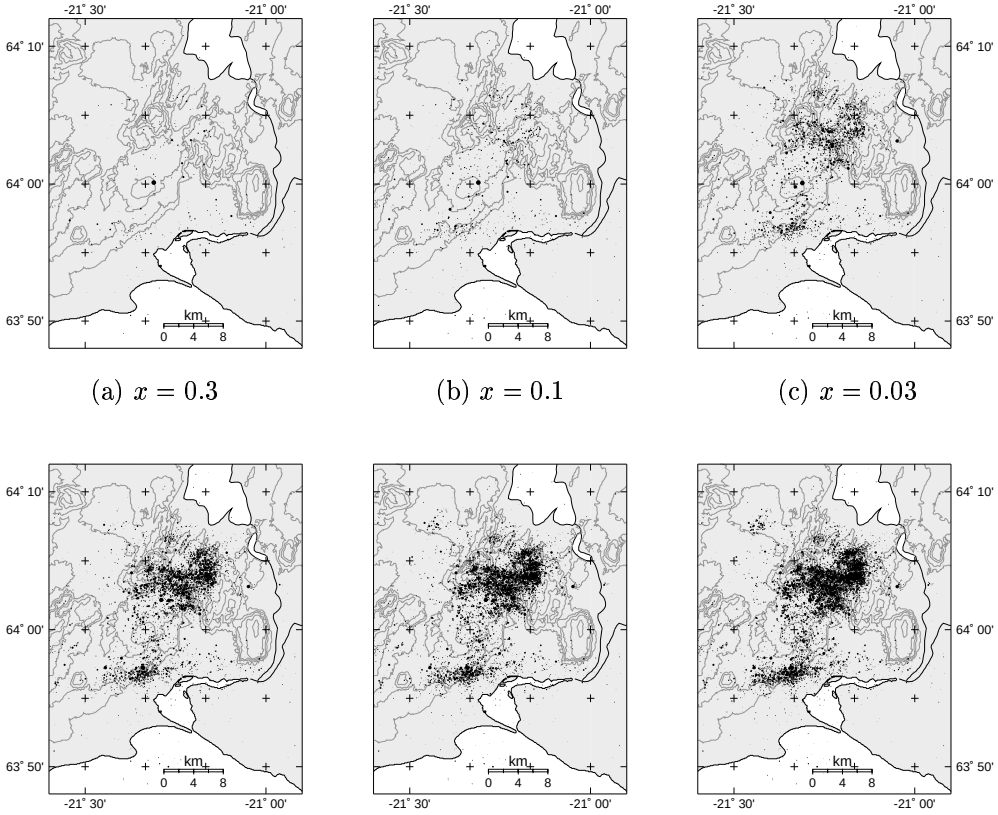

(a) $x = 0.3$ (b) $x = 0.1$ (c) $x = 0.03$

(d) $x = 0.01$ (e) $x = 0.003$ (f) $x = 0.001$

Figure 2.11: Independent seismicity as result of different choices of the parameter x

apparent in the independent part of the seismicity for $x < 0.1$ indicating that interaction mechanism have been neglected.

The plots of the dependent part of the seismicity in figure 2.12 does not show much differences in the results for the different parameters. This is due to the fact that the activity once found to be correlated for a high value of x will essentially remain correlated but in different clusters. Only the events at the cluster borders will disappear from the dependent seismicity. Figure 2.13 shows the number of independent and dependent events as a function of the parameter x.

In the following I want to analyze the shape of individual clusters in order to find a suitable value for the parameter x. Figures 2.14 to 2.16 show three selected clusters that represent different situations.

The first example I consider is the cluster defined by the large ($M_L = 5$)

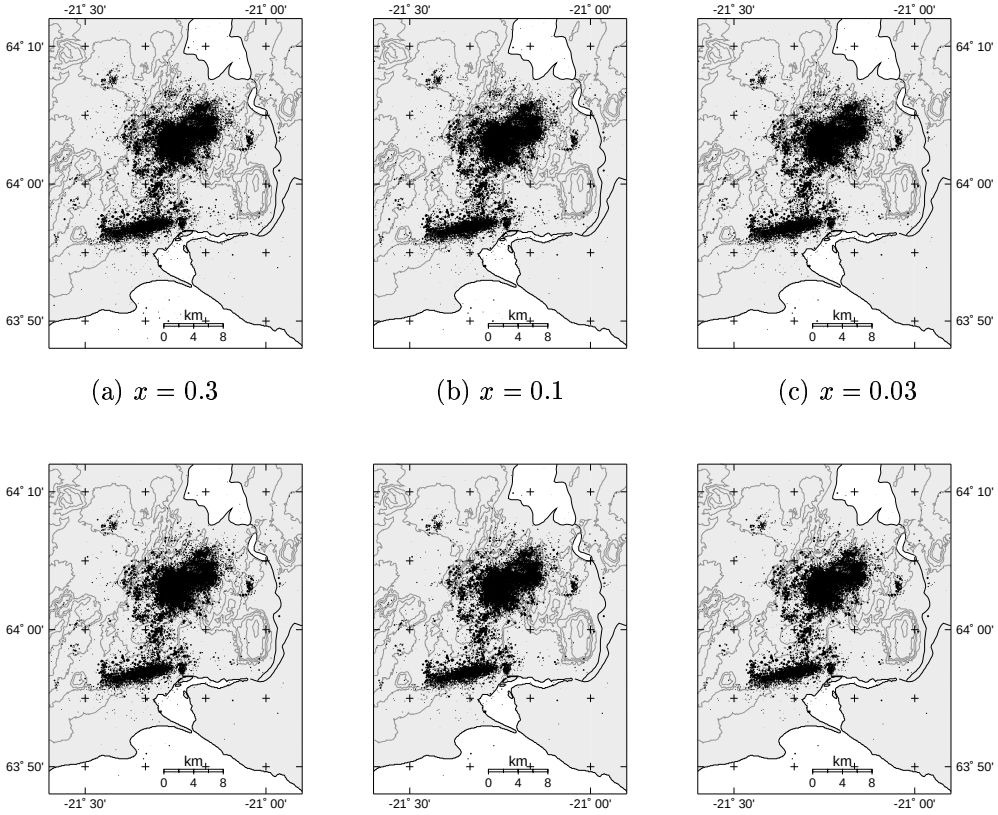

(a) $x = 0.3$ (b) $x = 0.1$ (c) $x = 0.03$

(d) $x = 0.01$ (e) $x = 0.003$ (f) $x = 0.001$

Figure 2.12: Dependent seismicity as result of different choices of the parameter x

earthquake from Nov 13 1998. This event triggered swarm earthquakes in a 10 to 15 km long E-W trending zone (Röngvaldsson et al., 1998). During this swarm activity in the Ölfus area there was ongoing activity around Mount Hengill to the north. Therefore this sequence offers a good opportunity to find a suitable range for x because on the one hand, following criterion three in chapter 2.1.3 the algorithm has to separate the Ölfus activity from the activity at Hengill. On the other hand the swarm activity lasts continuously for several weeks and thus requires a certain temporal duration of the cluster. The three columns of figure 2.14 show the results for $x = 0.03$, $x = 0.01$ and $x = 0.003$. The top row shows the clustered events in red and the whole activity during the period, displayed in the lower two columns, in black. The middle row shows the magnitude-time plots. The events that belong to the cluster are plotted red, the remainder activity is plotted in black. The bottom

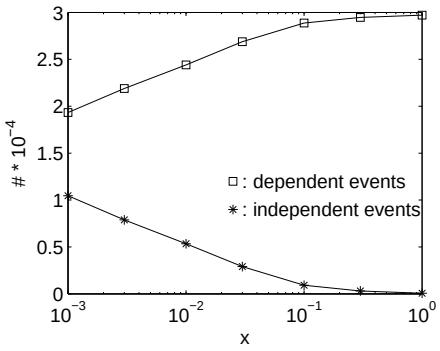

Figure 2.13: The number of dependent and independent events as identified by the algorithm as a function of the parameter x

row pictures the cumulative number of events in the respective time period. Again the red line belongs to the events in the cluster under consideration and the black line belongs to the whole activity.

The left row (figure 2.14(a)) shows the situation with too large x value. Events from all over the study area in the period from March 1997 until December 1999 are associated with the $M_L = 5$ event from Nov 13 1998. The cluster contains essentially all earthquakes that occurred in this period except some hundred swarm events that occurred between mid 1997 and mid 1998 as it can be seen in the lower two pictures of figure 2.14(a). The shape of the cluster obtained with a smaller x value of 0.01 or 0.003 is acceptable. The cluster contains the events in the Ölfus area and only a few from the Hengill region. This activity in the Hengill region started almost simultaneously with the Ölfus events and is therefor strongly correlated in time. Decreasing the value of x from 0.01 to 0.003 reduces the number of associated events form the Hengill region, but also leads to the loss of later events in the Ölfus area.

The second example I consider is the cluster identified by the $M_L = 5$ event from Jun 4 1998. The activity associated with this event is very interesting because of the stress transfer caused by it. There was very strong swarm activity in the Hengill region involving about 7000 events above $M_L = 0.5$ from April 1997 until the occurrence of this earthquake in the beginning of June 1998. After this quake the activity in the Hengill region faded away, but the Ölfus area experienced an activation culminating in the $M_L = 5$ event that marked the cluster considered above. The result for $x = 0.03$ in figure 2.15(a) is the same as in figure 2.14(a) because the two $M_L = 5$ events are correlated and the clusters thus identical. $x = 0.01$ separates the two $M_L = 5$ events and yields good results. The cluster contains the aftershock activity until the beginning of August 1998. A smaller x separates

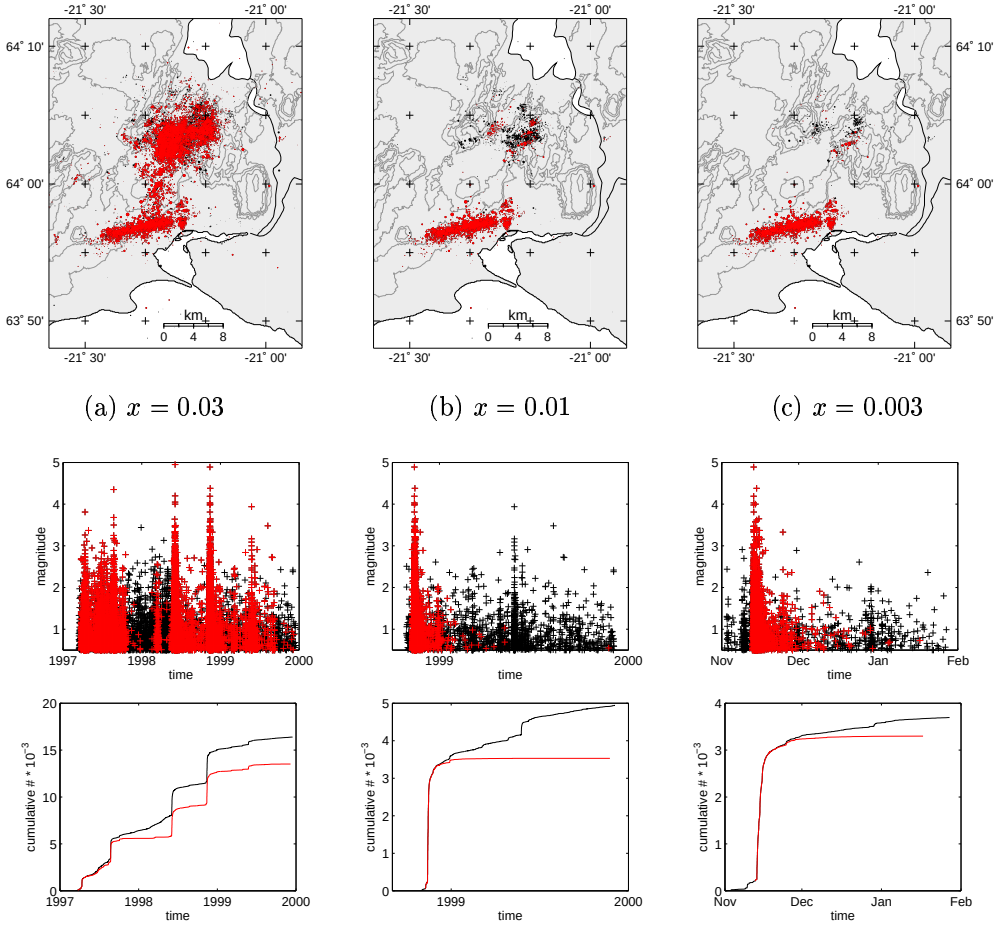

(a) $x = 0.03$ (b) $x = 0.01$ (c) $x = 0.003$

Figure 2.14: The cluster that contains the $M_L = 5$ event from Nov 13 1998 for different values of x

the cluster similarly but the aftershock activity contained in the cluster terminates already in the beginning of July (c.f. bottom row of figures 2.15(b) and 2.15(c)).

Since the last two examples belong to the two largest events in the dataset it was natural to analyze these clusters. Therefore I selected the $M_L = 3.3$ event from December 23 1993 arbitrarily to define the last example (figure 2.16). The activity in this period was comparably low and widely scattered. Only at the very beginning of January did clustered activity occur about $10km$ to the N-E. These events are separated for the displayed selection of x. A difference exists in the temporal extent. The small sequence following the $M_L = 2.2$ event from December 26 occurred at the same place as the one from December 23. This sequence is only contained in the cluster for

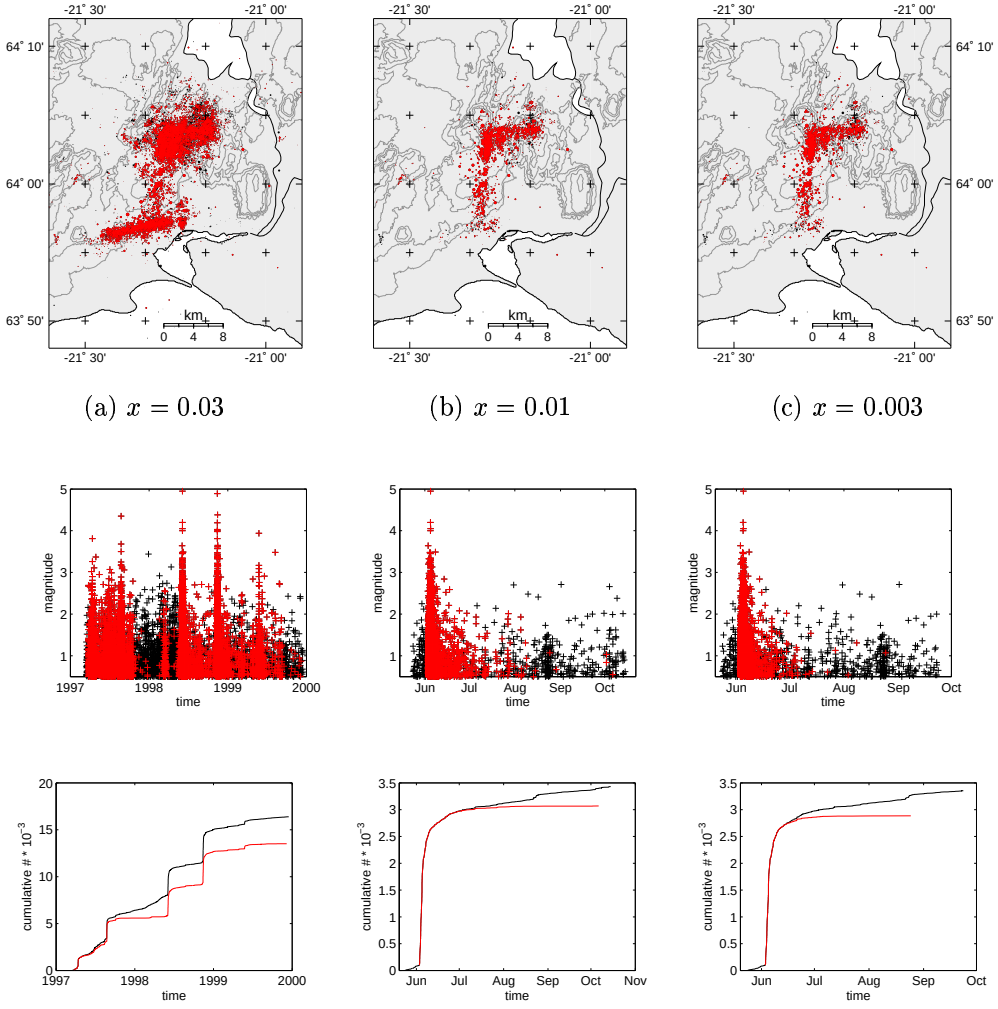

(a) $x = 0.03$ (b) $x = 0.01$ (c) $x = 0.003$

Figure 2.15: The cluster that contains the $M_L = 5$ event from Jun 4 1998 for different values of x

$x > 0.003$. The question as to whether this sequence should belong to the cluster illustrates the problem of choosing a scale for the clustering process.

After studying a number of clusters more, the value of $x = 0.01$ emerged as the best choice. This is because of two reasons. At first I wanted to separate the activity associated with the two $M_L \approx 5$ earthquakes from 1998. This is equivalent to excluding the large correlation scale that led to the apparent connection between these events. It is quite likely that motion on the plate boundary was a common source for at least part of the moment that was released in these earthquakes and thereby caused the correlation

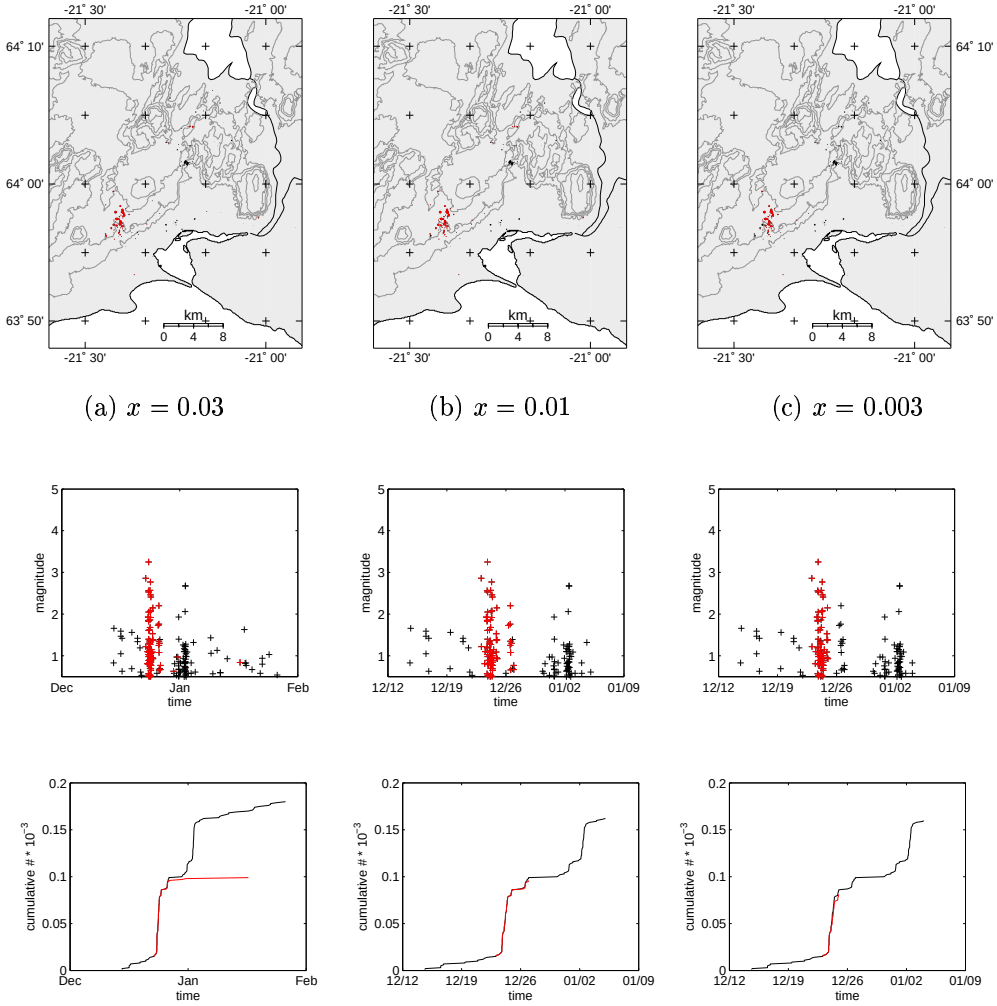

(a) $x = 0.03$ (b) $x = 0.01$ (c) $x = 0.003$

Figure 2.16: The cluster that contains the $M_L = 3.8$ event from December 23 1993 for different values of x

between them. For values of $x < 0.03$ these sequences are separated (c.f. 2.14(a) and 2.15(a)). The lower bound for a reasonable value for x is given by the temporal extent of correlated sequences, i.e. the clusters. Values of $x < 0.01$ exclude the correlation scales that link the activity within a fault on time scales of a few days or weeks (c.f. figure 2.16(c)).

2.2.5 Results

Using the value of $x = 0.01$ I applied the algorithm to the dataset without any restrictions to the magnitudes. I could verify the assumption that the shape of the clusters is effected very little by the small events below $M_L = 0.5$.

The temporal evolution of the dependent and independent seismicity as defined in section 2.1.3 is very informative concerning the quality of the declustering. In figure 2.17 the cumulative numbers of the dependent and independent parts are plotted versus time. It is can clearly shown that the

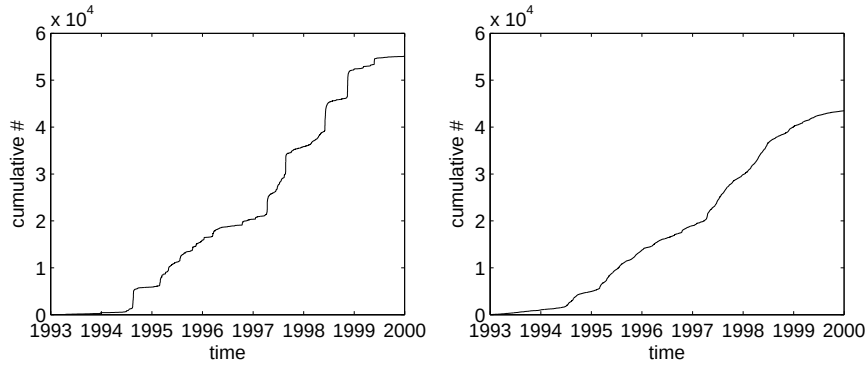

(a) Dependent seismicity (b) Independent seismicity

Figure 2.17: Cumulative numbers of events in the two parts of the seismicity

dependent events are strongly clustered in time. Its graph in figure 2.17(a) resembles a staircase which means that there are long periods without any dependent activity, and shorter periods with extremely high correlated activity. The independent seismicity represented by the smooth graph in figure 2.17(b) indicates a more or less random occurrence without any significant clustering as it is to be expected for uncorrelated events. The effect of the *strong* clustering, i.e. the limited correlation scale, is noticeable too because the independent events do not occur fully at random. The rate of independent events increases after mid 1994 and remains almost constant on a high level until the end of 1998 when it decreases again to the pre 1994 level. This indicates that there is a long scale correlation among the independent events between mid 1994 and end of 1998.

Figure 2.18(a) shows the size distribution of the clusters (cumulative number of clusters containing more events than N versus the number of events N in the cluster). The algorithm identified 38 clusters with more than 100 events and 20 clusters with more than 200 events. The locations of the clus-

ters with more than 200 events are marked by ellipsoids in figure 2.18(b).

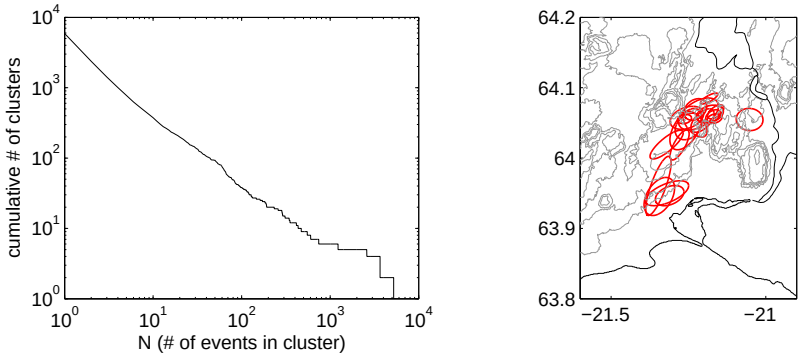

(a) Size distribution (b) Location

Figure 2.18: Size distribution and location of the 20 largest clusters

2.3 Summary

I tried two methods to decluster the catalogue. The conventional method followed the technique used by Reasenberg (1985). This method uses two free parameters to adopt the behaviour of the algorithm to the characteristics of the seismicity. It proved to be unsuitable for this dataset.

The statistical method developed on the basis of the unified scaling law for earthquakes (Bak et al., 2002) appeared to be better suited to this problem. Initially there is no free parameter in this method. To identify clusters on a certain space-time scale I introduced a parameter that governs the maximum scale of the correlation that link the events to form clusters. With a suitable choice of this parameter I obtained a set of clusters that meet the demands. For further analysis I will use the results of the statistical method.

Chapter 3

Parameters of individual clusters

In the last chapter I developed an algorithm that identifies sets of events that are strongly correlated in space and time, i.e. clusters. In this chapter I will estimate parameters that describe the seismicity in the 20 clusters that contain more than 200 events.

3.1 Patters in the temporal distribution

The temporal occurrence of earthquakes is dominated by clustering. In the case of aftershock sequences accompanying mainshocks this temporal clustering can be described by the Omori law (c.f. chapter 2.2.1) or the modified Omori law (MOL, Utsu et al., 1995)

$$R(t) = \frac{k}{(t+c)^p}. \tag{3.1}$$

Where $R(T)$ denotes the rate of earthquake occurrence at time t after the mainshock. k is a parameter related to the total number of aftershocks and the parameter c accounts for the complex effects directly after the mainshock. The parameter p governs the rate of the decay. The MOL states that the aftershock activity decays in time like a power law with the exponent p ranging between 0.3 and 2 (Davis and Frohlich, 1991; Kisslinger and Jones, 1991; Guo and Ogata, 1995). The evaluation of the exponent p suffers from the problem that one has to identify a unique mainshock. Often this is impossible because there is no unique way to classify a certain event as foreshock, mainshock or aftershock as many aftershocks act as mainshocks in that they trigger their own aftershocks.

One way to avoid this problem is the use of the epidemic type aftershock (ETAS) model (Ogata, 1999). The ETAS model is a generalization of the

MOL and takes into account the secondary aftershock sequences triggered by all pervious events. Thus this model treats every event as fore- main- and aftershock simultaneously. The inversion of this model on real data is difficult because it is analytically very complex and uses six parameters.

Another way to describe the temporal behaviour of seismicity by avoiding the identification of mainshocks is to use the time intervals between two successive events. The probability distribution of these waiting times $P(t_w)$ is defined in section 2.2.1. For correlated activity $P(t_w)$ has the form of a power law, i.e. $P(t_w) \propto t_w^{\alpha}$. In certain cases the two parameters p of the MOL and α of the waiting time distribution are related. If the activity can represented by a non-stationary Poisson process with the intensity proportional to t^{-p} the relation between the p-value and α is

$$-\alpha = 2 - p^{-1} \tag{3.2}$$

(Senshu (1959) in Hainzl et al. (2000)). The waiting time statistics thus offers an elegant way to quantify the temporal clustering, not only of earthquakes. Wheatland et al. (1998) for instance used the waiting time statistics to analyse the temporal correlation of solar flare bursts and Sánchez et al. (2002) analysed the waiting times of sandpile models. But it was also used for rainfall data, trades on stock markets and the temporal distribution of lightning.

In the context of earthquakes this concept has been used by Kagan and Jackson (1991), Christensen and Olami (1992), Hainzl et al. (2000), Hainzl (2003) and Bak et al. (2002).

3.1.1 Motivation

Hainzl (2003) investigated the effect of viscous coupling in a stick-slip block model. He introduced the viscous coupling in his model as transient stress redistribution to neighboring blocks after coseismic stress perturbation. Possible mechanism in real fault systems that could cause this relaxation process are fluid migration, afterslip or ductile creep. With increased viscous coupling that causes postseismic stress changes of the order of the coseismic changes Hainzl could reproduce typical features of earthquake swarms (Hainzl, 2003). The waiting time statistics was affected by the amount of postseismic response in a systematic way. The strength of the viscous coupling is quantified by the parameter f_p defined as the fraction of postseismic stress changes $f_p = \Delta\sigma_{post}/\Delta\sigma_{total}$. Figure 3.1 gives examples of waiting time distributions found by Hainzl (2003) in model simulations with viscous coupling of different strength. The parameter α[1] of the waiting time distri-

[1]The parameter α is called p_w by Hainzl (2003)

bution decreases from -1 in the case of weak ($f_p = 0.1$) to about -2 for strong viscous coupling ($f_p = 0.7$).

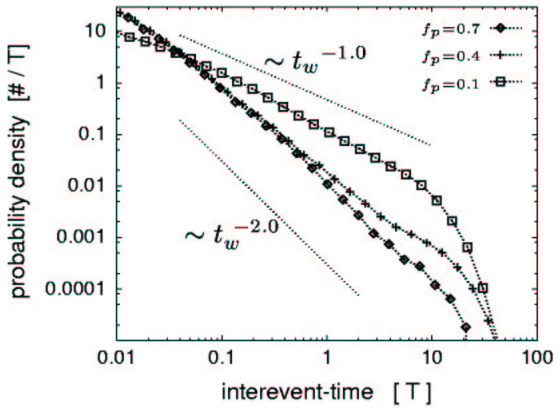

Figure 3.1: (*from Hainzl (2003)*) waiting time distributions for the model simulations with $f_p = 0.1$, 0.4 and 0.7.

Similarly to the waiting time distribution the size distribution represented by the Gutenberg-Richter b-value is systematically influenced by changes of the viscous coupling. This relation will be discussed in a later section.

On basis of this findings I want to draw conclusions on the influence of viscous effects in the Hengill region by analysing the waiting time statistics together with the size distribution of the clusters identified in chapter 2.2.

3.1.2 Estimation of α

For the measurement of the parameter α I calculate histograms of the waiting times. Because of the power law behaviour I use bins of logarithmically distributed width. The counts in the histogram c_i, with i being the index of the bin, are weighted according to

$$c_i = \frac{c_i^l}{w_i^l T \sum_i c_i}. \tag{3.3}$$

c_i^l denote the counts in the bins of logarithmically distributed width w_i^l in days. T denotes the times span of the analysed sequence also in days. The final histograms give the probability of finding an interevent time of length t_w within one day of observation normalised for the number of events that occur. The normalization for the number of events and the length of the

sequence is only done for comparison between different sequences. It has no influence on the value of α.

The parameter α is estimated as the slope of the least squares fit to the histogram in double logarithmic coordinates. For the least squares fit only waiting times larger than 40s are considered. As an estimate of the uncertainty of α I use the 95% confidence limit of the least squares fit. In figure 3.2 two examples of the waiting time distributions are shown.

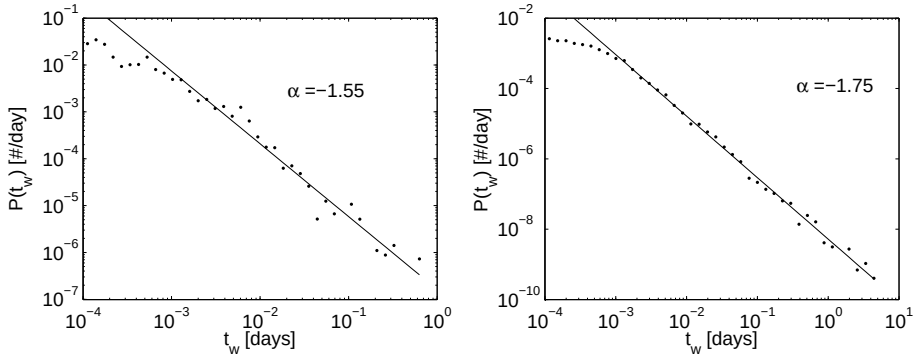

(a) cluster 13 (b) cluster 18

Figure 3.2: Examples of waiting time distributions for individual clusters

3.1.3 Results

I estimated α for 18 of the 20 cluster larger than 200 events. The power law regime in the two other clusters was to small for a reliable fit. The α-values are mapped on a colour scale and plotted as coloured ellipsoids at the location of the respective cluster in figure 3.3. In table C.1 the values together with the estimated uncertainties are given.

The α values scatter between -1.5 and -2 with an average uncertainty of 0.28. In the Ölfus area and the western part of the Hengill region α ranges between -1.5 down to -1.8. Four clusters show very low values below -1.8. In figure 3.4 the area of these clusters is indicated in blue together with the events that belong to them. These clusters are concentrated in a relatively small area $3km$ north of the uplift center with a diameter of approximately $6km$.

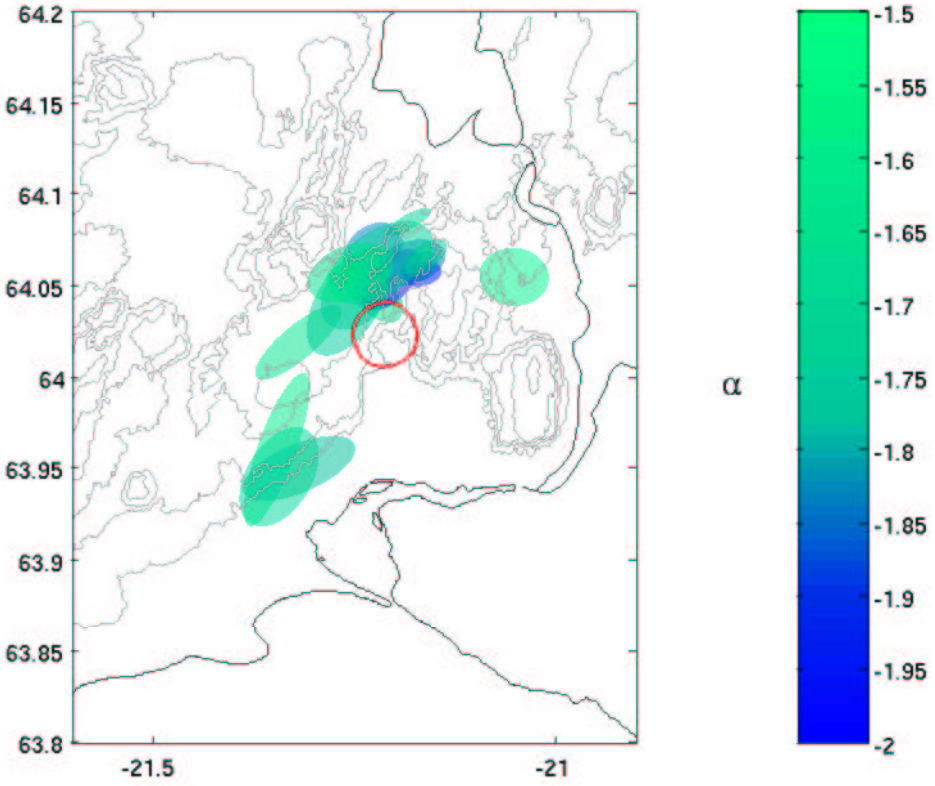

Figure 3.3: Spatial distribution of α value

3.2 Patterns in the size distribution

The size distribution of earthquakes is a typical example of scale invariance associated with a self-organized system (Bak and Tang, 1989). There is no characteristic size. Gutenberg and Richter (1944) first described the relation between the size of events and the frequency of their occurrence. This relation is known as the Gutenberg-Richter law (GRL) and was introduced in section 2.2.1. The parameter a in equation 2.5 is related to the total number of events and b determines the relation between large and small events. In contrast to the parameter a that varies simply with the size of the catalogue under study the b-value is almost constant at 1 if averaged over large volumes. On smaller scales of a few kilometers however considerable differences have been found (Wiemer and Wyss, 1997; Wiemer and Katsumata, 1999; Ogata and Katsura, 1993).

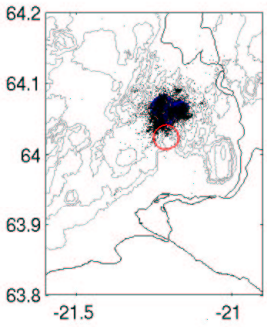

Figure 3.4: Clusters with $\alpha < -1.8$

3.2.1 Motivation

The GRL b-value was found to be related to the degree of structural heterogeneity in laboratory experiments (Mogi, 1962) and numerical simulations (Steacy et al., 1996). Wyss et al. (1997) studied the distribution of b-values in the surrounding of an active volcanoe and also attributed part of the variations to structural heterogeneities. These studies show a direct correlation between b and heterogeneity, i.e. b increases with increasing degree of heterogeneity.

Evidence for the influence of stress on the frequency-magnitude distribution come from laboratory tests (Scholz, 1968) and studies of mining induced seismicity (Urbancic et al., 1992). Wyss (1973) studied seismicity accompanying fluid injection experiments in Denver and also demonstrated a relation between stress and b. Comparison of b-values between thrusting and normal faulting environments (Frohlich and Davis, 1993) and the depth dependence of b (Wiemer and Wyss, 1997) give further evidence for this relation. The correlation between b and the stress level is indirect, i.e. high stress level causes low b-values.

As mentioned in section 3.1 Hainzl (2003) demonstrated the influence of viscous coupling on the frequency-size distribution in numerical models.

The variety of possible causes for perturbations of the frequency-magnitude distribution poses a problem for the interpretation. Better confidence in the conclusions drawn from certain properties of the b-values can be provided by a joint interpretation together with other parameters of the seismicity. Therefore I think Hainzl (2003) provides a good background for analysis of the frequency-magnitude distribution. In figure 3.5 frequency magnitude distributions of the simulations with different postseismic coupling by Hainzl (2003) are shown. There is a systematic increase in the b-value for increasing viscous coupling. b ranges from 0.7 in the case of weak coupling ($f_p = 0.1$)

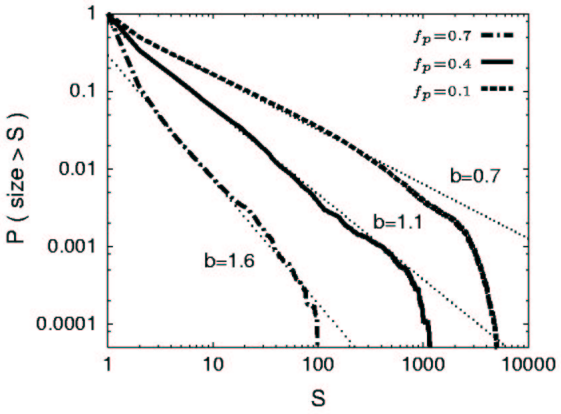

Figure 3.5: (*from Hainzl (2003)*) frequency-magnitude distributions for the model simulations with $f_p = 0.1$, 0.4 and 0.7.

to 1.6 for strong coupling with $f_p = 0.7$.

3.2.2 Estimation of b

There are two different ways to estimate the value of the parameter b in equation 2.5. The direct way makes use of the linear dependence of $\log_{10} N$ on the magnitude m. b can simply be estimated by a least squares fit as the slope of $\log_{10} N$ versus m. A requirement of this method is, that the graph to be fitted has a sufficiently large linear segment. Additionally this method is very sensitive to the number of large events which makes it rather unstable.

The indirect way uses the relation between the b-value and the mean magnitude. Aki (1965) showed that a maximum likelihood estimate for b is given by

$$b = \frac{0.4343}{< m > - m_c} \tag{3.4}$$

where m_c is the cutoff magnitude[2] and $< m >$ is the mean magnitude of events with magnitude greater than m_c. The approximate standard error δb of the b-value is given by $\delta b = \frac{b}{\sqrt{N}}$ (Aki, 1965) where N is the number of events used to estimate b. This method has two advantages. At first it does not require a strict power law shape of the frequency magnitude distribution. Thus one can not claim to directly measure some property of the scale invariant system, because the power law is the indicator of such

[2]The cutoff magnitude is the smallest magnitude that is completely reported in the catalogue.

systems. But the mean magnitude that is used for the maximum likelihood estimate still gives insight into the size distribution, i.e. ratio between large and small events. The second advantage is that the maximum likelihood estimate is very easy to calculate and very stable because the mean magnitude is dominated by the numerous small events rather than by the few large events.

3.2.3 Results

The b-value is estimated for the same clusters used in section 3.1. I obtained the b-values together with their standard errors using the maximum likelihood method. The magnitude cut m_c is set to $M_L = 0.5$ in accordance with Rögnvaldsson et al. (1998b) and the mean magnitude $< m >$ is calculated from local magnitudes. The results are again plotted as coloured ellipsoids at the clusters location in figure 3.6. The values together with their standard

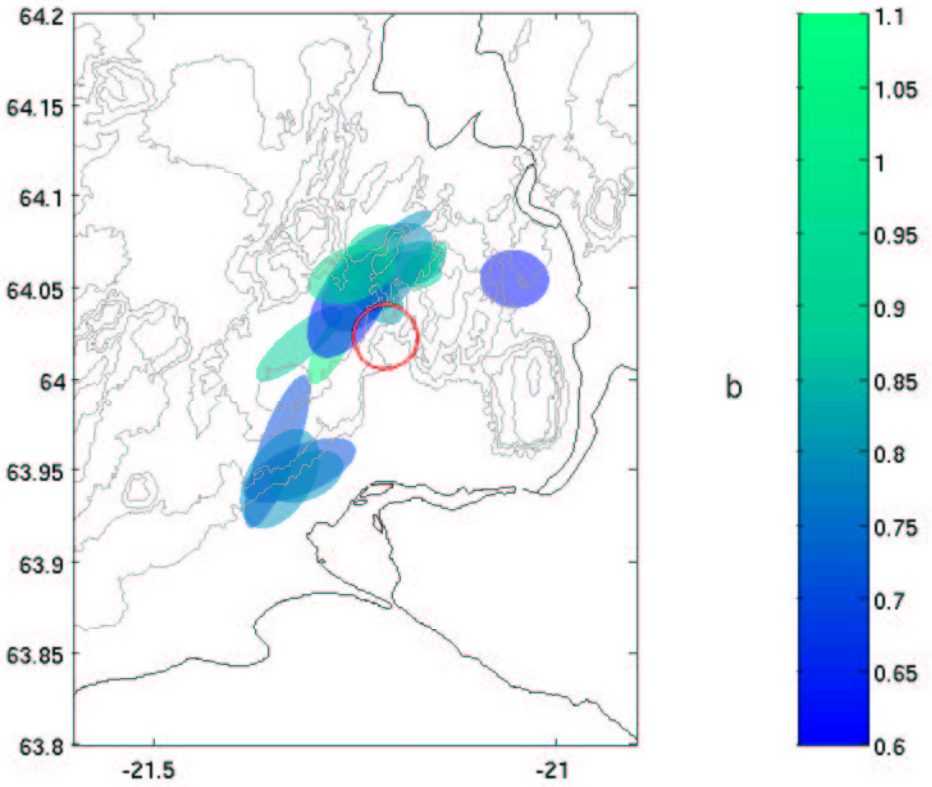

Figure 3.6: Spatial distribution of α value

error are given in table C.1. I found the b-values to range between 0.6 and 1.1 with a mean standard error of 0.1.

In the Ölfus area the values are more or less constant. Two clusters that occurred in 1995 (# 3 and 4) have $b = 0.79$ and the other two from 1997 and 1998 (# 15 and 19) have slightly lower values of $b = 0.7$. With respect to their error estimates the frequency-magnitude distribution of these four clusters can not be regarded different.

Except the cluster that contains the June 98 $M_L = 5$ earthquake (cluster # 18) the clusters in the closer vicinity of the uplift center show higher b-values. They range from 0.8 to 1.1. The value of cluster # 18 might be underestimated because the cluster contains an intensive aftershock sequence which might result in a temporally increased completeness level that would lower the b-value. In figure 3.7 the clusters with $b > 0.9$ are plotted. The

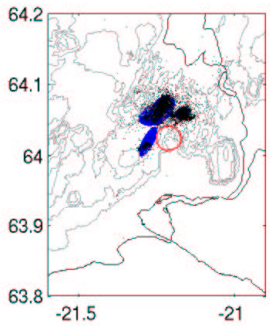

Figure 3.7: Clusters with $b > 0.9$

tendency to find the highest values around the uplift center suites to observations that link high b-values to areas of increased heterogeneity. Clifton et al. (2002) argue that the area to the north and west of the uplift center where I found the highest b-values is the area of greatest structural complexity. This causes the seismic activity to be concentrated north and west of the uplift though the assumed point source produces a circular stress field.

3.3 Joint interpretation of α and b distributions

The interpretation of individual seismicity parameters suffers from ambiguity. This can partly be overcome by interpreting different parameters together. This approach of course requires the knowledge about the effects of a certain cause on different parameters. The most effective way to gain this kind of knowledge is to use numerical simulations where one has complete control on

individual parameters. In natural systems the actual cause of an observed effect is often hidden in a combination of several possible causes.

As mentioned in previous sections Hainzl (2003) modeled the effect of viscous coupling on the waiting time distribution and the frequency-size distribution in numerical simulations. Hence this study provides means to jointly interpret α and b-values.

Increased viscous coupling is according to Hainzl (2003) accompanied by high b-value and low α-value (cf. figures 3.1 and 3.5). The numerical simulations do not really provide a way to quantify high or low values. The values can thus only be quantified in relation to each other or in relation to their mean.

I decided to declare the largest 25% of the b-values as large in the sense discussed above and the smallest 25% of the α-values as small. This results in 4 clusters with *low* α values and 5 clusters with *high* b-values. The threshold values resulting from this definition are -1.8 for the α and 0.9 for the b-value.

The clusters that fulfill these conditions separately are plotted in figures 3.4 and 3.7. The clusters number 14 and 20 fulfill these conditions simultaneously their location is shown in figure 3.8. These are the clusters that are, according to the observations of Hainzl (2003), most affected by viscose coupling.

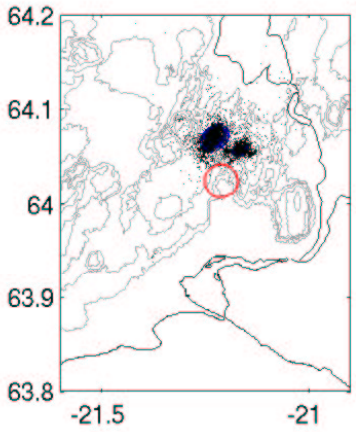

Figure 3.8: Clusters with $b > 0.9$ and $\alpha < -1.8$

3.4 Spatial patterns, Configurational Entropy

Patterns in the spatial distribution of earthquakes strongly reflect the processes and structures inside the earth. Earthquakes follow the delineation of plate boundaries, the distribution of faults or they are coupled to magmatic activity. The amount of clustering of the earthquake distribution varies significantly, geographically as well as over time. Often the shape and size of these earthquake clusters provides information about the processes involved.

The concept of fractality or multifractality is one way to characterise the composition of earthquake distributions. To calculate a fractal dimension requires scale-invariance of the epicentral distribution over length scales of several magnitudes. This is often problematic for earthquakes since the length scales are limited by the extent of the tectonic regime on one side and the spatial resolution, i.e. the location errors of the network on the other side.

The concept of configurational entropy provides an alternative way to quantify the statistical properties of a point set. It aims at the description of the interplay between ordered features and scatter in the distribution. In the context of earthquakes configurational entropy has successively been used to measure the random scatter in the epicentral distribution that is caused by location errors (Nicholson et al., 2000). They used the entropy to measure the improvement of earthquake locations made by a technique called collapsing method. Simply speaking the collapsing method enhances the order in the hypocenters by moving them in a suitable direction inside their error ellipsoids. Similarly entropy can be used to quantify the improvements of other relocation techniques such as joint hypocenter or master event relocations.

Nicholson et al. (2000) also show that the entropy of earthquake distributions in different tectonic environments such as mid-oceanic ridges, subduction zones and intraplate zones varies significantly.

Goltz and Böse (2002) used the entropy to demonstrate similarities between the phase transition at the critical point in a percolation model on the one hand and the Southern California earthquake population in the spatial and temporal vicinity of the 1992 Landers earthquake. As for the percolation model at the percolation threshold[3] they find the entropy of the southern California earthquake to increase prior to the Landers event, to reach its maximum at the event and to decrease slowly afterwards.

[3]The percolation threshold represents the critical point where the phase transition from impermeable to permeable occurs.

3.4.1 Motivation

By measuring the entropy of the clusters I identified in section 2.2 I want to test whether it is possible to classify the clusters according to spatial distribution of their events. Secondly I want to analyse the temporal evolution of the entropy to see whether there is any significant change in the characteristic of the hypocenter distribution and whether the two $M_L \approx 5$ events from 1998 are reflected in the entropy.

3.4.2 Definition of S

The classical concept of entropy in thermodynamics introduced in 1871 by Boltzmann was extended to be applicable in information theory by Shannon (1948). He defined the information I that we gain from the occurrence of event $i (i = 1, 2, \ldots, n)$ as

$$I_i = \ln \frac{1}{P_i} \tag{3.5}$$

where p_i is the probability for the occurrence of this event. The entropy S of a system is the expected value of I as

$$S = \sum_{i=1}^{n} P_i I_i = -\sum_{i=1}^{n} P_i \ln P_i \tag{3.6}$$

(Shannon, 1948).

The meaning of Shannon's entropy for a 2D point set, like the epicenters of earthquakes, can be understood as follows. Considering a discretised image of a certain number of pixels the information gained if we get to know that an event occurred at pixel i depends on the probability p_i. If $p_i = 1$ i.e. the event was certain to occur in cell i the information gained is $-\ln p_i = 0$. Whereas I is infinite if $p_i = 0$. S will adopt its maximum if all p_i are equal, i.e. when there is maximum disorder (Goltz, 1998).

If the probability is a continuous function of space rather than a piecewise constant, equation 3.6 can be written as

$$S = -\int_V P(x) \ln(P(x)) dx \tag{3.7}$$

(cf. Papoulis (1984) in Nicholson et al. (2000)) where x is the position vector in the domain V. To overcome the problem equivalent to the one known from thermodynamics that a reference temperature is needed to define an absolute value and not only differences of the entropy, Skilling (1989) generalized equation 3.7 to incorporate a reference distribution m:

$$S = -\int_V P(x) \ln \left(\frac{P(x)}{m(x)} \right) dx \tag{3.8}$$

(cf. Skilling (1989) in Nicholson et al. (2000)) with m and P being normalized probability densities. For a set of points the probability $P(x)$ is related to the local density $\rho(x)$ by

$$P(x) = \frac{\rho(x)}{N} \tag{3.9}$$

where N is the number of points. Using equation 3.9 in equation 3.8 results in

$$S = \ln(N) - \frac{1}{N}\int_V \rho(x)\ln(\rho(x))dx + \frac{1}{N}\int_V \rho(x)\ln(m(x))dx \tag{3.10}$$

Equation 3.10 shows that the entropy can be calculated if the spatial distribution of the point density is known. The problem of estimating the local point density can be tackled with different techniques. One group of these techniques requires the use of some arbitrary smoothing parameters which often have strong influence on the density estimate. The domain of the point set can for instance be divided up into boxes of side length L which gives an estimate for the density via the number of points in each box. The smoothing parameter in these box-counting methods is the box size L. Too large boxes reduce the resolution and too small boxes increase the error. Goltz and Böse (2002) estimate the point densities for various box sizes and finally use the box size that yields the maximum entropy to avoid these arbitrariness of the smoothing parameter.

A quite different technique, introduced by Nicholson et al. (2000), makes use of Voronoi cells. Because this method does not require any smoothing parameter I use this technique and follow the work of Nicholson et al. (2000).

The Voronoi diagram is a unique partition of the domain into nearest-neighbor region of a set of points (referred to as nodes). Each region contains those points that are nearer to one node than to any other. Figure 3.9 shows the Voronoi diagram of the $M_L > 2$ events in the Hengill region. It is obvious in figure 3.9 that the size of the Voronoi cells reflects the density of the point set. The idea of Nicholson et al. (2000) was to use the inverse of the size of the Voronoi cell as density estimate of its interior:

$$\rho(x) = \frac{1}{v(x_i)}. \tag{3.11}$$

x_i is the position vector of the ith node and $v(x_i)$ denotes the volume of the Voronoi cell about node i. x_i is assumed to be the closest node to the position vector x which means that x lies within cell i. Equation 3.11 provides a unique measure of the local point density without the use of any smoothing

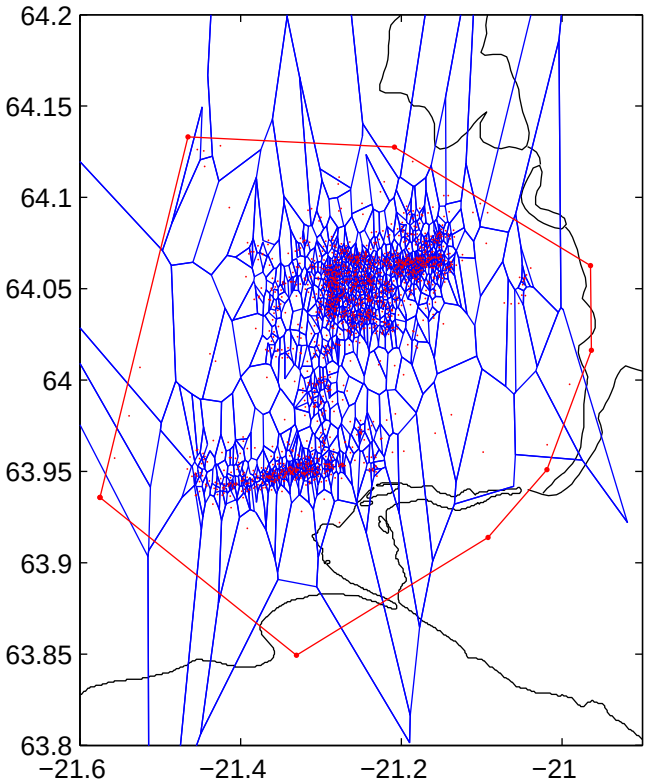

Figure 3.9: Voronoi diagram (blue lines) of the $M_L > 2$ events (red points). Red line indicates the convex hull of the epicenters.

parameter. The Voronoi cells of the nodes that belong to the convex hull[4] of the point set pose a problem because they are unbounded which leads to zero point density. Thus only the volume inside the convex hull is considered for the estimation of the density. The sum of all cell volumes then becomes equal to the volume of the convex hull V_0.

The integrals in equation 3.10 can be replaced by sums because the Voronoi diagram covers the domain and the density is piecewise constant. Using equation 3.11 this gives:

$$S = \ln(N) + \frac{1}{N}\sum_{i=1}^{N}\ln(v_i) + \frac{1}{N}\sum_{i=1}^{N}\ln(m_i(x)). \tag{3.12}$$

The differentials dx in equation 3.10 become v_i in equation 3.12.

[4]A set S is *convex* if for any given points $p, q \in S$ the line segment $\overline{pq} \subseteq S$.The *convex hull* of a set of points Q is the intersection of all convex sets containing Q, i.e. the convex hull of Q is the smallest convex set that contains Q.

A natural choice for the reference distribution is, to make it uniform and structureless. This results in a constant probability

$$m_i = \frac{1}{V_0}. \tag{3.13}$$

With this choice the maximum entropy value is the one of a uniform distribution which is zero. All other distributions will have negative entropy (Nicholson et al., 2000). Using this reference distribution and equation 3.12 one finally obtains

$$S = \ln(N) - \ln(V_0) + \frac{1}{N}\sum_{i=1}^{N}\ln(v_i). \tag{3.14}$$

The entropy definition in equation 3.14 has several interesting properties (cf. Nicholson et al., 2000).

- S is always non-positive.
- S is scale invariant. (A factor that scales all volume terms cancels.)
- S is normalised for the number of events N and the volume of the domain V_0.

The entropy can thus be compared between sets with different numbers of events that occupy vastly different volumes.

3.4.3 Estimation of S

The estimation of S according to formula 3.14 involves the following steps

1. Coordinate transformation from geographical into Cartesian coordinates
2. Calculation of the Voronoi diagram
3. Calculation of the intersection between the convex hull of the set and each Voronoi cell
4. Calculation of the volume of each of these intersections between hull and Voronoi cell from 3 and of the convex hull itself
5. Calculation of S by using the volumes obtained in 4 in equation 3.14

I used the GMT software by Wessel and Smith (1991) for the coordinate transformation in item 1. For the calculation of the Voronoi diagram in item 2 I made use of the *qhull* program released by the National Science and Technology Research Center for Computation and Visualization of Geometric Structures (The Geometry Center), University of Minnesota (1993). It is based on the *quickhull* algorithm (Barber et al., 1996) for calculating convex hulls. I used the same program to calculate the intersection in item 3 and the volume in item 4.

I tested the algorithm on sets of uniformally distributed points in a unit cube. Table 3.1 gives the entropies of these test distributions. The entropy

# of points	# on conv. hull	Volume	Entropy
100	30	0.673	−0.8073
100	27	0.693	−0.1114
100	28	0.709	−1.5253
1000	78	0.890	−0.1578
1000	77	0.914	−0.1658
1000	63	0.938	−0.2096
10000	112	0.990	−0.1225
10000	119	0.986	−0.1112
10000	101	0.987	−0.1136
100000	196	0.998	−0.1028

Table 3.1: Entropy values for test distributions of 10000 uniformally distributed point in a unit cube

of the sets with 100 points scatters comparatively wide around a mean of -0.81. The range of the scatter decreases with increasing number of points in the sets and the mean increases to -0.18 for the sets with 1000 points and to -0.12 for the sets containing 10000 points.

This nicely fulfills the expectations for the entropy estimate. The entropy approaches zero as the number of points increases because any structure that is left in smaller sets vanishes and the uniformity becomes dominant. The larger variations for smaller sets reflect the fact that small sets badly reflect the statistical properties of the distribution they were drawn from. Conversely one can not distinguish between large sets from the same distribution from the statistical point of view.

I am thus very confident in the quality of the algorithm.

3.4.4 Results

I estimated the entropy S of the 20 largest clusters i.e. the same used in sections 3.1 and 3.2. In figure 3.10 the entropy values are plotted in the same fashion as the α and b-values in sections 3.1.3 and 3.2.3. The exact

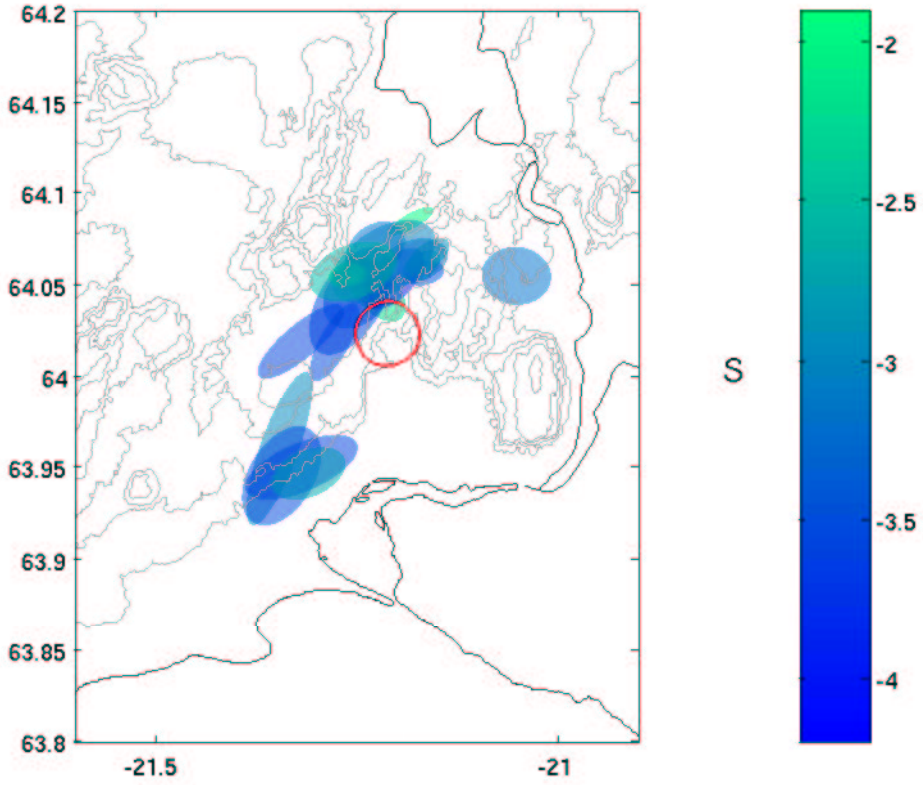

Figure 3.10: Spatial distribution of entropy S

values are given in table C.1. The entropy values range between -1.9 and -4.1. There is no clear systematics evident in the spatial distribution of entropy. However the entropy of the clusters in the Hengill area averages to -2.9 whereas the Ölfus clusters have slightly lower average of -3.3. Because of the large scatter of the values I calculated S for all events with $M_L > 0.5$ to the north and south of 64° latitude. These values mirror the averaged values of the clusters very nicely. I found $S = -2.85$ for the events north of 64° corresponding to an cluster average of -2.9 and $S = -3.21$ for the events south of 64° corresponding the -3.3. This shows that the activity in the Hengill area tends to be more diffuse than in the Ölfus region.

Nicholson et al. (2000) estimated values of S for seismicity in 10 different tectonic regions. They found values of S between -4.26 and -3.88 for mid-oceanic ridges, between -3.84 and -2.73 for subduction zones and a range from -2.78 to -1.75 for continental regions. Thus the values for the clusters in the Hengill region can not be classified according to this because they occupy almost the whole range and also classification of the values for Hengill and Ölfus is not very instructive as both fall in the range of subduction zones. However it seems not surprising to find the higher entropy in the Hengill region that surely has some intraplate characteristics in opposite to the Ölfus area that probably has transform characteristics as it is the westward continuation of the SISZ.

There is one problem with this concept of entropy that appeared during my work. Equation 3.14 includes a normalisation of the entropy with respect to the size of the domain. This arose from the reference distribution that was used to fix the value of zero entropy. But still I found some correlation between the extent of the set and its entropy which is related to the insufficient scale invariance of the epicenter distribution. On a scale of e.g. 20 km (cf. figure 1.2) one can intuitively separate active and inactive areas. This means structure. If the extent of the set used to estimate entropy is placed on this boundary between active and inactive areas this structure disappears and the entropy increases. The value of S thus correlates with the size of the "inactive" volume, that typically surrounds some concentrated activity, inside the convex hull of the set.

Temporal analysis of S

I used this observation to improve the analysis of the temporal evolution of entropy. For this the entropy is calculated for time windows of different length. The windows contain 300 events and have an overlap of 50 events. I used the convex hull of the whole set of events for each time window because of the problem mentioned above. Figure 3.11 shows the entropy evolution from January 1998 to July 1999. This period is selected because of the two $M_L \approx 5$ events.

The two $M_L \approx 5$ events are clearly reflected in the entropy (cf. figure 3.11). S assumes local maxima around both large events. This is in accordance with the results of Goltz and Böse (2002) for the M 7.3 Landers event in Southern California. The entropy maximum at the occurrence of the mainshock is interpreted by Goltz and Böse (2002) as indication of a phase transition and critical point dynamics that take place at the mainshock. I can confirm that the seismicity, temporally related to the $M_L \approx 5$ events, shows maximum disorder. The exponential increase of S prior to the mainshocks

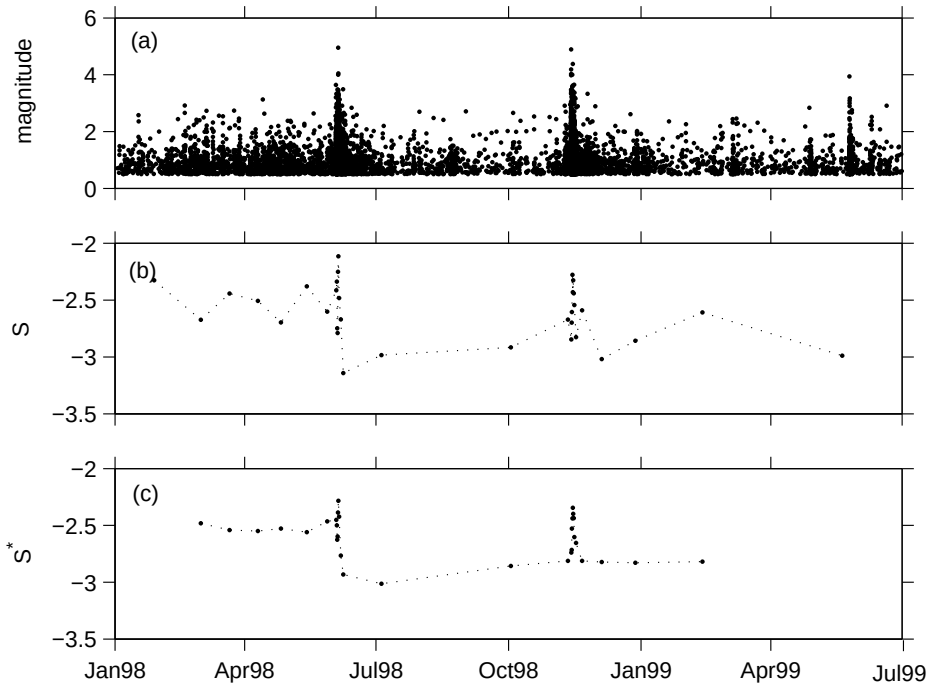

Figure 3.11: Temporal evolution of entropy. (a) time-magnitude plot, (b) entropy plotted at the center of time window, (c) entropy smoothed with a centered moving average filter of 3 points length

as described by Goltz and Böse (2002) could not be found in this dataset, excluding a forecasting potential for the Hengill area.

I applied a centered moving average filter of length 3 to the time series of S. The result S' displayed in figure 3.11 (c) shows that there is a difference of about 20% between the average values before and after the June event. This jump can be interpreted as change in the characteristics of seismicity. The system probably moved away from the critical state (Main and Al-Kindy, 2002) because the $M \approx 5$ event might have decreased the stress level of the whole area significantly as it transfered strain to the plate boundary.

Chapter 4

Summary and Conclusions

In this work I analysed patterns in the distribution of earthquakes in space, time and magnitude. This was done in two steps documented in chapters 2 and 3.

In the first part I developed a method to identify clusters of strongly correlated events. 20 clusters were found that contain more than 200 events. These clusters represent temporally dense accumulations of events in a narrow region e.g. a fault. The method is based on a certain form of the correlations between earthquakes expressed by the recently found Unified Scaling Law (Bak et al., 2002). During the analysis I could verify the Unified Scaling Law and show that there are differences in the properties of the earthquake correlations between the Hengill area and the Southern California seismicity analysed by Bak et al. (2002).

In the second part I studied different properties of the seismicity in the individual clusters. I estimated three parameters for each cluster, the α-value of the interevent time distribution and b-value of the frequency-magnitude distribution and the configurational entropy S describing the degree of spatial clustering.

Significant differences between different clusters were found in the α and b-value. b-values range between 0.6 and 1.1 and α-values were found between -1.5 and -2. With the interpretation of these results I follow the findings of Hainzl (2003) who describe an influence of the viscous coupling on the frequency-magnitude and interevent time distributions. The pattern that indicate strong viscous effects could be localized below the Hrómundartindur central volcano in an area directly to the north of the uplift center determined by Feigl et al. (2000). The high b-values that were found in the Hengill-Hrómundartindur area might reflect strong heterogeneity. Clifton et al. (2002) argue that this heterogeneity caused the concentration of seismicity north and west of the uplift center though one would expect at least

some kind of rotational symmetry for a point like source.

I speculate that the increased postseismic response north of the uplift center is caused by fluids that originated from the magma injection and migrated into the direction of high heterogeneity.

Comparison between the entropy values of the different clusters did not reveal an obvious systematic. The values range between -1.9 and -4.1. However a tendency to lower entropy in the Ölfus clusters compared to the Hengill-Hrómundartindur clusters was noticeable. This observation could be confirmed by separate analysis of the whole seismicity north and south of 64° latitude. In the view of Goltz and Böse (2002); Main and Al-Kindy (2002) where a system assumes its maximum entropy at the critical point the higher entropy in the Hengill-Hrómundartindur area indicates that this system was in a state closer to criticality than the Ölfus system. Temporal evolution of the entropy between January 1998 and July 1999 showed maxima at the occurrence of the two $M_L \approx 5$ events in June and November 1998 and a drop in entropy from pre June level at -2.5 to a post June level at about -3. This entropy drop occurred simultaneously with the event that mechanically linked the Hengill-Hrómundartindur system to the plate boundary. I think the entropy jump in June 1998 reflects a significant change in character of the seismicity in the Hengill-Hrómundartindur system away from criticality.

Bibliography

Aki, K. (1965). Maximum likelihood estimate of b in the formula $\log N = a - bm$ and its confidence. *B. Earthq. Res. I. Tokyo*, 43:237–239.

Bak, P., Christensen, K., Danon, L., and Scanlon, T. (2002). Unified Scaling Law for Earthquakes. *Phys. Rev. Lett.*, 88:178501.

Bak, P. and Tang, C. (1989). Earthquakes as a self-organized critical phenomenon. *J. Geophys. Res.*, 94:15635–15637.

Barber, C., Dobkin, D., and Huhdanpaa, H. (1996). The Quickhull Algorithm for Convex Hulls. *ACM Trans. Math. Software*, 22:469–483.

Böðvarsson, R., Rögnvaldsson, S., Jakobsdóttir, S., Slunga, R., and Sefánsson, R. (1996). The SIL data aquisition and monitoring system. *Seismol. Res. Lett.*, 67:35–46.

Christensen, K. and Olami, Z. (1992). Variation of the Gutenberg-Richter b values and nontrivial temporal correlations in a spring-block model for earthquakes. *J. Geophys. Res.*, 97:8729–8735.

Clifton, A., Sigmundsson, F., Feigl, K., Guðmundsson, G., and Árnadóttir, T. (2002). Surface effects of faulting and deformation resulting from magma accumulation at the Hengill triple junction, SW Iceland, 1994-1998. *J. Volcanol. Geoth. Res.*, 115:233–255.

Cox, S. and Scholz, C. (1988). On the formation and growth of faults: an eyperimental study. *J. Struct. Geol.*, 10:413–430.

Davis, S. and Frohlich, C. (1991). Single-link cluster analysis of earthquake aftershocks: decay laws and regional variations. *J. Geophys. Res.*, 96:6335–6350.

DeMets, C., Gordon, R., Argus, D., and Stein, S. (1994). Effect of recent revisions to the geomagnetic reversal time scale on estimate of current plate motions. *Geophys. Res. Lett.*, 21:2191–2194.

Einarsson, P. (1991). Earthquakes and present-day tectonism in Iceland. *Tectonophysics*, 189:261–279.

Einarsson, P. and Eiríksson, J. (1982). Earthquake fractures in the districts Land and Rangárvellir in the South Iceland Seismic Zone. *Jökull*, 32:113–120.

Einarsson, P. and Sæmundsson, K. (1987). *Earthquake epicenters 1982-1985 and volcanic systems in Iceland (map)*. Í hlutarins eðli: Festschrift for Th. Sigurgeirsson. Menningarsjóður, Reykjavík.

Feigl, K., Gasperi, G., Sigmundsson, F., and Rigo, A. (2000). Crustal defomation near Hengill volcano, Iceland 1993-1998: Coupling between magmatic activity and faulting inferred from elastic modeling of satellite radar interferrograms. *J. Geophys. Res.*, 105:25655–25670.

Fischer, T. and Horálek (2002). Space – Time Distribution of Earthquake Swarms in the Principal Focal Zone of the NW Bohemia/Vogtland Seismoactive Region: Period 1985-2001. *J. Geodyn.*

Frohlich, C. and Davis, S. (1990). Single-link cluster analysis as a method to evaluate spatial and temporal properties of earthquake catalogues. *Geophys. J. Int.*, 100:19–32.

Frohlich, C. and Davis, S. (1993). Teleseismic *b* values: Or, much ado about 1.0. *J. Geophys. Res.*, 98:631–644.

Gardner, J. and Knopoff, L. (1974). Is the sequence of earthquakes in southern California, with aftershocks removed, Poissonian? *Bull. Seismol. Soc. Am.*, 64:1363 – 1367.

Goltz, C. (1998). *Fractal and Chaotic Properties of Earthquakes*, volume 77 of *Lecture notes in earth sciences*. Springer.

Goltz, C. (2001). Decomposing spatio-temporal seismicity patterns. *Natural Hazards and Earth System Sciences*, 1:82–92.

Goltz, C. and Böse, M. (2002). Configurational entropy of critical earthquake populations. *Geophys. Res. Lett.*, 29:51/1–4.

Gripp, A. and Gordon, R. (1990). Current plate velocities relative to the hotspots incorporating the NUVEL-1 global plate motion model. *Geophys. Res. Lett.*, 17:1109–1112.

Guðmundsson, A. (1987). Tectonics of the Thingvellir fissure swarm, SW Iceland. *J. Struct. Geol.*, 9:61–69.

Guo, Z. and Ogata, Y. (1995). Correlations between characteristic parameters of aftershock distributions in time, space and magnitude. *Geophys. Res. Lett.*, 22:993–996.

Gutenberg, R. and Richter, C. (1944). Frequency of earthquakes in California. *Bull. Seismol. Soc. Am.*, 34:185–188.

Hainzl, S. (2003). Self-organzation of earthquake swarms. *J. Geodyn.*, 1-2:157–172.

Hainzl, S., Zöller, G., and Kurths, J. (2000). Self-organization of spatio-temporal earthquake clusters. *Nonlinear Proc. Geoph.*, 7:21–29.

Kagan, Y. and Jackson, D. (1991). Long-term earthquake clustering,. *Geophys. J. Int.*, 104:117–133.

Kagan, Y. Y. (1999). Universality of the Seismic Moment-frequency Relation. *Pure Appl. Geophys.*, 155:537 – 573.

Kisslinger, C. and Jones, L. (1991). Proreties of aftershock sequences in Southern California. *J. Geophys. Res.*, 96:11947–11958.

Lay, T. and Wallace, T. C. (1995). *Modern Global Seismology*, volume 58 of *International Geophysics Series*. Academic Press.

Main, I. (1999). Is the reliable prediction of individual earthquakes a realistic scientific goal? URL: `http://www.nature.com/nature/debates/earthquake/equake_frameset.html`. Debates in nature.

Main, I. and Al-Kindy, F. (2002). Entropy, energy and proximity to criticality in global earthquake populations. *Geophys. Res. Lett.*, 29:25/1–4.

Mogi, K. (1962). Magnitude-frequency relation for elastic shocks accompanying fractures of various materials and some related problems in earthquakes. *Bull. Earthq. Res. Inst. Tokyo Univ.*, 40:831–853.

Mogi, K. (1969). Some features of recentseismic activityin and near Japan{2}, activity before and after great earthquakes. *Bull. Earthq. Res. Inst. Tokyo Univ.*, 47:395–417.

Nicholson, T., Sambridge, M., and Gudmundsson, O. (2000). On entropy and clustering in earthquake hypocenter distributions. *Geophys. J. Int.*, 142:37–51.

Ogata, Y. (1999). Seismicity analysis through Point-process Modeling: A Review. *Pure Appl. Geophys.*, 155:471–507.

Ogata, Y. and Katsura, K. (1993). Analysis of temporal and spatial heterogeneties of the magnitude frequency distribution inferred from earthquake catalogues. *Geophys. J. Int.*, 113:727–738.

Okubo, P. and Aki, K. (1987). Fractal Geometry in the San Andreas Fault System. *J. Geophys. Res.*, 92:345–355.

Pagli, C., Pedersen, R., Sigmundsson, F., and Feigl, K. (2003). *Triggered aseismic fault slip on the Reykjanes peninsula, Iceland captured by radar interferometry*, volume 5 of *Geophysical Research Abstracts*, page 06434. European Geophysical Society.

Papoulis, A. (1984). *Probability, Random Variables and Stocastic Processes.* McGraw-Hill, New York, 2nd edition.

Reasenberg, P. (1985). Second-Order Moment of Central California Seismicity, 1969-1982. *J. Geophys. Res.*, 90:5479 – 5495.

Rögnvaldsson, S., Guðmundsson, A., and Slunga, R. (1998a). Seismotectonic analysis of the Tjörnes Fracture Zone, an active transform fault in north Iceland. *J. Geophys. Res.*, 103:30117–30129.

Rögnvaldsson, S., Guðmundsson, G., Águstsson, K., Jakobsdóttir, S., Slunga, R., and Stefánsson, R. (1998b). *Overview of 1993-1996 seismicity near Hengill*, volume VÍ-R98006-JA05 of *Rit Veðurstofu Íslands.* Veðurstofa Íslands, Reykjavík.

Röngvaldsson, S., Árnadóttir, T., Águstsson, K., Skaftadóttir, T., Guðmundsson, G., Björnsson, G., Vogfjörð, K., Stefánsson, R., Böðvasson, R., Slunga, R., Jakobsdóttir, S., Thorbjarnardóttir, B., Erlendsson, P., Bergsson, B., Ragnarsson, S., Halldórsson, P., Thorkelsson, B., and Asgeirsdóttir, M. (1998). *Skjálftahrina í Ölfusi í nóvember*, volume VÍ-R98006-JA05 of *Greinargerð.* Veðurstofa Íslands, Reyhjavík. Icelandic with English summary.

Sæmundsson, K. (1986). *Subaerial volcanism in the western North Atlantic*, volume M of *The Geology of North America*, chapter 5. Geol. Soc. Am.

Sæmundsson, K. (1995). *Hengill, geological map (bedrock) 1:50000.* Orkustofnun and Hitaveita Reykjavíkur and Landmælingar Íslands, Reykjavík.

Sánchez, R., Newman, D., and Carreras, B. (2002). Waiting-Time Statistics of Self-Organized-Criticality Systems. *Phys. Rev. Lett.*, 88:068302.

Savage, W. U. (1972). Microearthquake clustering near Fairview Peak, Nevada, and in the Nevada seismic zone. *J. Geophys. Res.*, 77:7049 – 7056.

Scholz, C. (1968). The frequency-magnitude relation of microfracturing in rock and its relation to earthquakes. *Bull. Seismol. Soc. Am.*, 58:399–415.

Senshu, T. (1959). On the time interval distribution of aftershocks. *Zisin*, 12:149–161.

Shannon, C. (1948). A Mathematical Theory of Communication. *Bell Syst. Tech. J.*, 27:379–423 and 623–656.

Shearer, P. (1999). *Introduction to Seismology*. Cambride Univ. Press, Cambridge.

Sigmundsson, F., Einarsson, P., Rögnvaldsson, S., Foulger, G., Hodgkinson, K., and Thorbergsson, G. (1997). The 1994-1995 seismicity and deformation at the Hengill triple junction, Iceland: Triggering of earthquakes by minor magma injection in a zone of horizontal shear stress. *J. Geophys. Res.*, 102:15151–15161.

Skilling, J. (1989). *Maximum entropy and Bayesian Methods*, pages 45–52. Kluwer Academic, London.

Steacy, S., McCloskey, J., Bean, C., and Ren, J. (1996). Heterogeneity in a self-organized critical earthquake model. *Geophys. Res. Lett.*, 23:383–386.

Stefánsson, R., Böðvarsson, R., Slunga, R., Einarsson, P., Jakobsdóttir, S., Bungum, H., Gregersen, S., Havskov, J., Hjelme, J., and Korhonen, H. (1993). Earthquake prediction research in the South Iceland Seismic Zone and the SIL Project. *Bull. Seismol. Soc. Am.*, 83:696–716.

Stein, S. and Wysession, M. (2003). *Introduction to Seismology, Earthquakes, and Earth Structure*. Blackwell Publishing.

Tiampo, K. (2002). Mean-field threshold systems and phase dynamics: An application to earthquake fault systems. *Europhys. Lett.*, 60:481–487.

Urbancic, T., Trifu, C., Long, J., and R.P., T. (1992). Space -time correlations of b values with stress release. *Pure Appl. Geophys.*, 139:449–462.

Utsu, T., Ogata, Y., and Matsu'ura, R. (1995). The centenary of the Omori formula for a decay law of aftershock activity. *J. Phys. Earth*, 43:1–33.

Vogfjöð, K. (2003). *Triggered seismicity after the June 17, $M_w = 6.5$ earthquake in the South Iceland Seismic Zone: The first five minutes*, volume 5 of *Geophysical Research Abstracts*, page 11251. European Geophysical Society.

Wessel, P. and Smith, W. (1991). Free software helps map and display data. *EOS Trans. AGU*, 72:441.

Wheatland, M., Sturrock, P., and McTieman, J. (1998). The Waiting-Time Distribution of Solar Flare Hard X-Ray Bursts. *Astrophys. J.*, 509:448.

Wiemer, S. and Katsumata, K. (1999). Spatial variability of seismicity parameters in aftershock zones. *J. Geophys. Res.*, 104:13135 – 13151.

Wiemer, S. and Wyss, M. (1997). Mapping the frequency-magnitude distribution in asperities: An improved technique to calculate recurrence times? *J. Geophys. Res.*, 102:15115–15128.

Wyss, M. (1973). Towards a physical understanding of the earthquake frequency distribution. *Geophys. J. Roy. Astr. S.*, 31:341–359.

Wyss, M., editor (1999). *Seismicity Patterns, their Statistical Significance and Physical Meaning*, volume 155 of *Pure Appl. Geophys.* Birkhäuser Verlag AG.

Wyss, M., Shimazaki, K., and Wiemer, S. (1997). Mapping active magma chambers by b values beneath the off-Ito volcano, Japan. *J. Geophys. Res.*, 102:20413–20422.

Zöller, G. and Hainzl, S. (2001). Detecting premonitory seismicity patterns based on critical point dynamics. *Natural Hazards and Earth System Sciences*, 1:93–98.

Appendix A

The declustering process

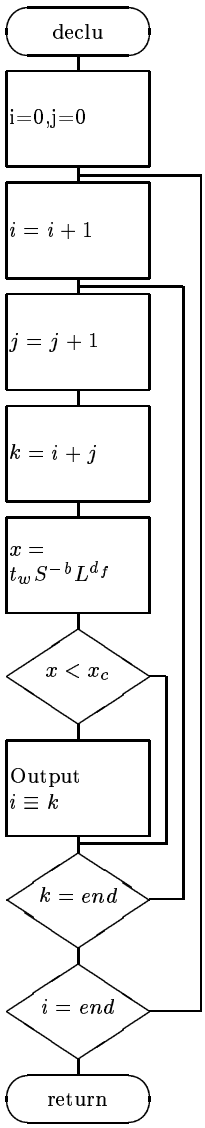

The declustering algorithm described in section 2.2.2 works according to the following flowchart.The program starts at the top and works downward. Diamond shaped objects denote decisions and the program works downward if the condition is true, and otherwise to the right. i, j and k denote indices of events in the catalogue and *end* is the number of events in the catalogue. The $\equiv$ sign symbolises that the events are associated.

Appendix B

Point distributions

The mean distance between two random point drawn from a uniform distribution in a plane can be estimated in numerical simulations. I simply generate 100000 pairs of uniformally distributed points in a square of side length 1. The distribution of the distances between the points of these pairs is plotted in figure B.1(a). The mean distance is 0.5214.

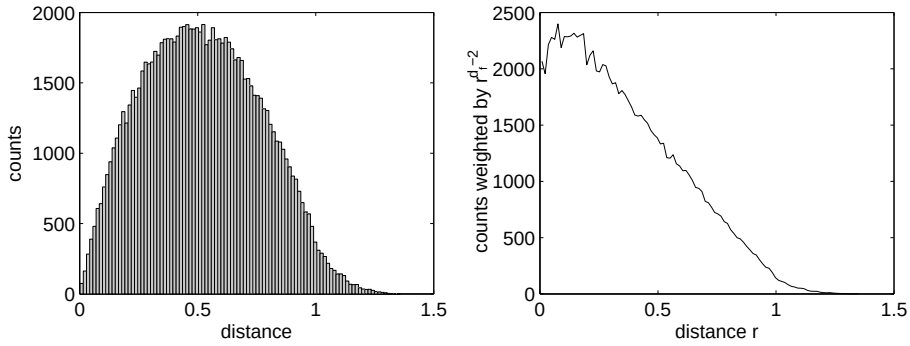

(a) uniform distribution (b) fractal distribution

Figure B.1: The distribution of distances between points in a plane for different kinds of point distributions.

To simulate the distance distribution between pairs of points of a fractal set I use the distribution shown in figure B.1(a) and apply a weighting factor for the different bins that account for the clustering caused by the fractality. On a set of points with a fractal distribution the number of points N inside a sphere of radius r is $N(r) \propto r^{d_f}$. The probability $P(r)$ of finding a point at distance r, $P(r) \propto r^{d_f-1}$ is proportional to the derivative of $N(R)$. The

fraction of the probabilities $P_f(r)$ for the fractal distribution $P_u(r)$ for the uniform distribution of dimension 2 is:

$$\frac{P_f(r)}{P_u(r)} \propto \frac{r^{d_f-1}}{r^{2-1}} = r^{d_f-2}. \tag{B.1}$$

This is the weighting factor to be applied to the bins in the histogram in figure B.1(a). Figure B.1(b) shows the weighted histogram that represents the distribution of distances between points on a fractal set of dimension 1.1. The mean distance between two points is 0.36 in this case where 100 bins were used.

Appendix C

Results

#	time	# of events	b-value	α-value	entropy
1	13/08/94 – 28/08/94	3667	0.81 ± 0.04	-2.03 ± 0.31	-4.1
2	26/02/95 – 01/03/95	603	0.84 ± 0.1	-1.84 ± 0.23	-3.3
3	02/03/95 – 04/03/95	435	0.79 ± 0.13	-1.69 ± 0.29	-3.6
4	14/03/95 – 15/03/95	310	0.79 ± 0.13		-2.7
5	08/04/95 – 10/04/95	285	0.83 ± 0.15	-1.68 ± 0.27	-1.9
6	30/04/95 – 04/05/95	743	0.88 ± 0.11	-1.69 ± 0.24	-2.9
7	22/07/95 – 24/07/95	472	0.8 ± 0.13	-1.69 ± 0.32	-3.1
8	26/07/95 – 29/07/95	345	0.98 ± 0.16	-1.62 ± 0.27	-2.5
9	22/10/95 – 24/10/95	415	0.92 ± 0.12	-1.72 ± 0.32	-2.4
10	16/11/95 – 17/11/95	233	0.89 ± 0.22	-1.63 ± 0.31	-3.6
11	12/01/96 – 13/01/96	287	0.8 ± 0.14	-1.69 ± 0.29	-1.9
12	14/03/96 – 17/03/96	259	0.82 ± 0.13	-1.6 ± 0.3	-2.2
13	14/10/96 – 20/10/96	552	0.61 ± 0.11	-1.55 ± 0.21	-3.2
14	12/04/97 – 17/04/97	2594	0.95 ± 0.07	-1.83 ± 0.26	-3.2
15	10/07/97 – 11/07/97	291	0.7 ± 0.17	-1.61 ± 0.23	-3.0
16	23/08/97	352	1.09 ± 0.23		-3.5
17	24/08/97 – 06/09/97	3668	0.82 ± 0.04	-1.76 ± 0.25	-3.5
18	03/06/98 – 01/08/98	5578	0.61 ± 0.02	-1.75 ± 0.25	-3.6
19	12/11/98 – 18/12/98	5214	0.7 ± 0.03	$-1.79 \pm .24$	-3.7
20	25/05/99 – 01/06/99	1228	0.91 ± 0.1	-1.97 ± 0.36	-3.5

Table C.1: Parameters of the seismicity in different clusters

The numbers of the clusters in table C.1 refer to ellipsoids labeled with the cluster numbers in figure C.1.

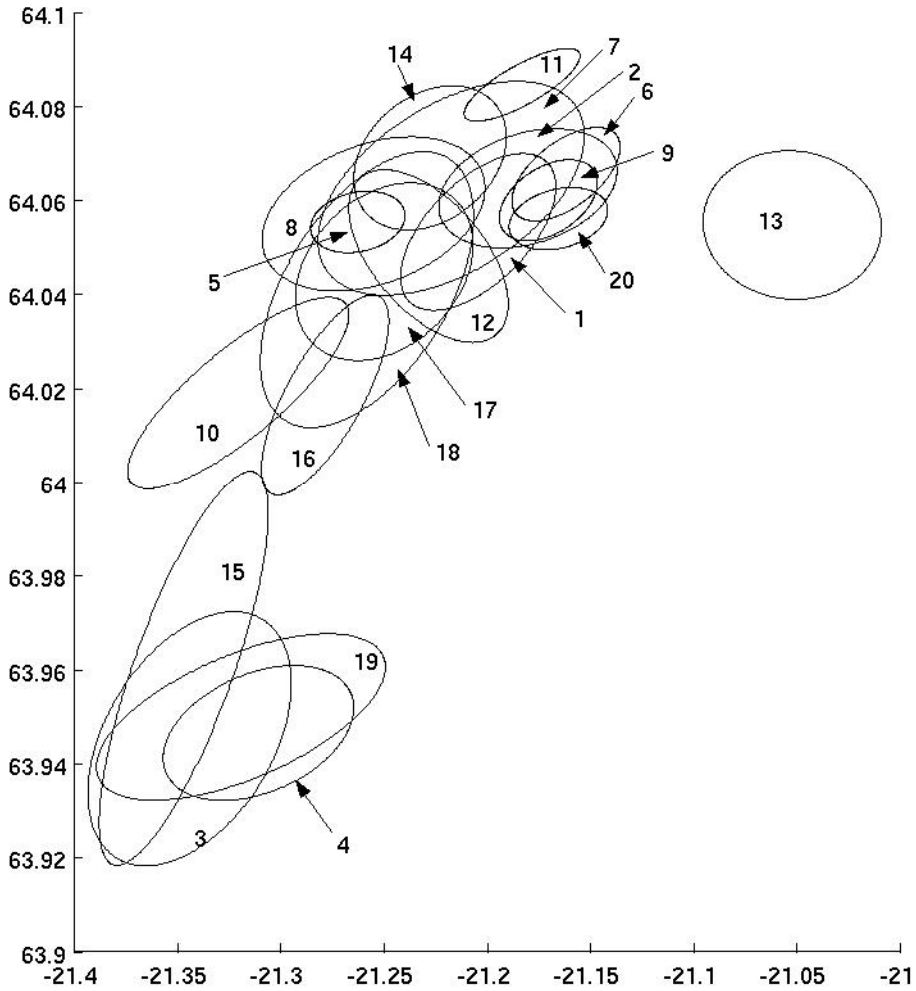

Figure C.1: Cluster numbers

Statement of Authenticity

I hereby declare that I alone have written the attached document with only the help of the mentioned resources.

Date, Signature

Upon positive assessment this document may be placed at the disposal of the library of the Institute of Geophysics and Geology, University of Leipzig.

Date, Signature